

B. Bhushan  
*Editor*

NANOSCIENCE AND TECHNOLOGY

# Scanning Probe Microscopy in Nanoscience and Nanotechnology

---

Volume 3



Springer

*Editor*

Professor Bharat Bhushan

Ohio State University

Nanoprobe Laboratory for Bio- and Nanotechnology and Biomimetics (NLB<sup>2</sup>)

Columbus, Ohio

USA

*Series Editors:*

Professor Dr. Phaedon Avouris

IBM Research Division

Nanometer Scale Science & Technology

Thomas J. Watson Research Center

Yorktown Heights, NY

USA

Professor Dr. Bharat Bhushan

Ohio State University

Nanoprobe Laboratory

for Bio- and Nanotechnology  
and Biomimetics (NLB<sup>2</sup>)

Columbus, Ohio

USA

Professor Dr. Dieter Bimberg

TU Berlin, Fakultät Mathematik/

Naturwissenschaften

Institut für Festkörperphysik

Berlin

Germany

Professor Dr., Dres. h.c. Klaus von Klitzing

Max-Planck-Institut

für Festkörperforschung

Stuttgart

Germany

Professor Hiroyuki Sakaki

University of Tokyo

Institute of Industrial Science

4-6-1 Komaba, Meguro-ku

Tokyo 153-8505, Japan

Professor Dr. Roland Wiesendanger

Institut für Angewandte Physik

Universität Hamburg

Hamburg

Germany

**NanoScience and Technology** ISSN 1434-4904

ISBN 978-3-642-25413-0 ISBN 978-3-642-25414-7 (eBook)

DOI 10.1007/978-3-642-25414-7

Springer Heidelberg New York Dordrecht London

Library of Congress Control Number: 2009934500

© Springer-Verlag Berlin Heidelberg 2013

This work is subject to copyright. All rights are reserved by the Publisher, whether the whole or part of the material is concerned, specifically the rights of translation, reprinting, reuse of illustrations, recitation, broadcasting, reproduction on microfilms or in any other physical way, and transmission or information storage and retrieval, electronic adaptation, computer software, or by similar or dissimilar methodology now known or hereafter developed. Exempted from this legal reservation are brief excerpts in connection with reviews or scholarly analysis or material supplied specifically for the purpose of being entered and executed on a computer system, for exclusive use by the purchaser of the work. Duplication of this publication or parts thereof is permitted only under the provisions of the Copyright Law of the Publisher's location, in its current version, and permission for use must always be obtained from Springer. Permissions for use may be obtained through RightsLink at the Copyright Clearance Center. Violations are liable to prosecution under the respective Copyright Law.

The use of general descriptive names, registered names, trademarks, service marks, etc. in this publication does not imply, even in the absence of a specific statement, that such names are exempt from the relevant protective laws and regulations and therefore free for general use.

While the advice and information in this book are believed to be true and accurate at the date of publication, neither the authors nor the editors nor the publisher can accept any legal responsibility for any errors or omissions that may be made. The publisher makes no warranty, express or implied, with respect to the material contained herein.

Printed on acid-free paper

Springer is part of Springer Science+Business Media ([www.springer.com](http://www.springer.com))

Urheberrechtlich geschütztes Material

# NANO SCIENCE AND TECHNOLOGY

---

# NANO SCIENCE AND TECHNOLOGY

---

*Series Editors:*

P. Avouris B. Bhushan D. Bimberg K. von Klitzing H. Sakaki R. Wiesendanger

The series NanoScience and Technology is focused on the fascinating nano-world, mesoscopic physics, analysis with atomic resolution, nano and quantum-effect devices, nano-mechanics and atomic-scale processes. All the basic aspects and technology-oriented developments in this emerging discipline are covered by comprehensive and timely books. The series constitutes a survey of the relevant special topics, which are presented by leading experts in the field. These books will appeal to researchers, engineers, and advanced students.

Please view available titles in *NanoScience and Technology* on series homepage  
<http://www.springer.com/series/3705/>

Bharat Bhushan  
Editor

# Scanning Probe Microscopy in Nanoscience and Nanotechnology

3

With 419 Figures

- J.P. Carmo** Algoritmi Center, University of Minho, Azurem, Guimaraes, Portugal
- P.A. Carvalho** NanoLab – Nanostructured Materials and Nanotechnologies Laboratory, Instituto Superior Técnico, Technical University of Lisbon, Lisbon, Portugal
- Andres Castellanos-Gomez** Kavli Institute of Nanoscience, Delft University of Technology, Delft, the Netherlands
- R. Colaço** NanoLab – Nanostructured Materials and Nanotechnologies Laboratory, Instituto Superior Técnico, Technical University of Lisbon, Lisbon, Portugal
- J.H. Correia** Algoritmi Center, University of Minho, Azurem, Guimaraes, Portugal
- Etienne Dague** CNRS UPR8001, LAAS, Toulouse, France
- Antonio José Felix de Carvalho** Escola de Engenharia de São Carlos, University of São Paulo (USP) – Campus São Carlos, São Carlos – São Paulo, Brazil
- Frank W. DelRio** Material Measurement Laboratory, National Institute of Standards and Technology, Gaithersburg, MD, USA
- Ali Dirani** Institut de Sciences des Materiaux de Mulhouse – IS2M, CNRS LRC 7228, Mulhouse, France
- Martin L. Dunn** Department of Mechanical Engineering, University of Colorado, Boulder, CO, USA
- Robert H. Eibl, M.D.** Institute of Pathology, Technical University of Munich, Munich, Germany
- Tamara Elzein** Equipe Chimie et Physico-Chimie des Polymères – Enscmu, Université de Haute Alsace, Mulhouse, France
- Ille C. Gebeshuber** Institute of Applied Physics, Vienna University of Technology, Wien, Austria
- L.M. Gonçalves** Algoritmi Center, University of Minho, Azurem, Guimaraes, Portugal
- Hakan Göçerler** AC2T Research GmbH, Austrian Center of Competence for Tribology, Neustadt, Austria
- Hamidou Haidara** Institut de Sciences des Materiaux de Mulhouse – IS2M, CNRS LRC 7228, Mulhouse, France
- Philip Hemmer** 214 Zachry Engineering Center, Electrical Engineering, Texas A&M University, College Station, TX, USA
- Markus Hund** Lehrstuhl für Physikalische Chemie II, Universität Bayreuth, Bayreuth, Germany

**Neil H. Thomson** Molecular and Nanoscale Physics Group, School of Physics and Astronomy, University of Leeds, Leeds, UK

**Agnieszka Tomala** AC2T Research GmbH, Austrian Center of Competence for Tribology, Neustadt, Austria

**Larisa Tsarkova** Lehrstuhl für Makromolekulare Materialien und Oberflächen (IPC) Pauwelsstraße 8, DWI an der RWTH Aachen e.V., Aachen, Germany

**Michael Urbakh** Orenstein 207, School of Chemistry, Tel-Aviv University, Tel Aviv, Israel

**Ugo Valbusa** Nanomed Lab, Physics Department, UNIGE

Nanobiotechnologies, National Institute for Cancer Research IST, Genova I, Italy

**Stefan A.L. Weber** Max-Planck-Institute for Polymer Research, Mainz, Germany

**Fabio Minoru Yamaji** University of São Carlos (UFSCar) – Campus Sorocaba, São Paulo, Brazil

**Huiliang Zhang** Harvard-Smithsonian Center for Astrophysics, Cambridge, MA, USA

**Yin Zhang** State Key Laboratory of Nonlinear Mechanics (LNM), Institute of Mechanics, Beijing, China

**Ya-pu Zhao** State Key Laboratory of Nonlinear Mechanics (LNM), Institute of Mechanics, Beijing, China

**Part III Industrial Applications**

<b>15 Atomic Force Microscopy in Bioengineering Applications .....</b>	<b>397</b>
R. Colaço and P.A. Carvalho	
15.1 Introduction.....	397
15.2 Fundamentals of the AFM .....	400
15.2.1 Working Principles .....	400
15.2.2 Resolution .....	402
15.2.3 Probe Selection .....	403
15.3 Imaging .....	404
15.3.1 Contact Mode .....	404
15.3.2 Dynamic Modes .....	405
15.4 Nanotribology, Nanomechanics, and Force Spectroscopy .....	407
15.4.1 Nanotribology.....	407
15.4.2 Nanomechanical Properties .....	407
15.4.3 Force Spectroscopy .....	412
15.5 Imaging Applications in Bioengineering.....	416
15.6 Nanotribological Experiments in Biomaterials Using the AFM ...	418
15.7 Nanomechanical Characterization of Biomaterials and Biological Structures .....	420
15.8 Conclusions .....	425
References .....	425
<b>16 Bridging Nano- and Microtribology in Mechanical and Biomolecular Layers .....</b>	<b>431</b>
Agnieszka Tomala, Hakan Göçerler, and Ille C. Gebeshuber	
16.1 Introduction to Nanotribology and Microtribology .....	432
16.1.1 Monomolecular Thin Films .....	433
16.1.2 Additive-Derived Reaction Layers .....	434
16.1.3 Hard Coatings.....	435
16.1.4 Biomolecular Layers .....	435
16.2 Experimental Approach .....	439
16.2.1 AFM .....	439
16.2.2 AR-XPS .....	445
16.2.3 Microtribometer .....	447
16.3 Results and Discussion .....	452
16.3.1 Monomolecular Thin Films .....	452
16.3.2 Tribocochemical Additive-Derived Reaction Layer .....	455
16.3.3 Hard Coatings.....	460
16.3.4 Biomolecular Layers: Tribological Investigation on Human Stratum Corneum Epidermis Using Atomic Force Microscopy .....	462

<b>16.3.5</b>	<b>Staining Experiments Related to the Interactions Between Contact Lenses and Ocular Tissues</b>	<b>473</b>	
<b>16.4</b>	<b>Conclusion and Outlook: Bridging the Gap.....</b>	<b>479</b>	
	<b>References</b>	<b>480</b>	
<b>17</b>	<b>Thin Films for Thermoelectric Applications .....</b>	<b>485</b>	
	M.F. Silva, J.F. Ribeiro, J.P. Carmo, L.M. Gonçalves, and J.H. Correia		
<b>17.1</b>	<b>Introduction.....</b>	<b>485</b>	
<b>17.1.1</b>	<b>Thermoelectricity .....</b>	<b>486</b>	
<b>17.1.2</b>	<b>Thermoelectric Devices .....</b>	<b>488</b>	
<b>17.1.3</b>	<b>Motivation .....</b>	<b>493</b>	
<b>17.2</b>	<b>Thermoelectricity.....</b>	<b>494</b>	
<b>17.2.1</b>	<b>Thermoelectricity Theory .....</b>	<b>494</b>	
<b>17.2.2</b>	<b>Thermoelectric Materials .....</b>	<b>502</b>	
<b>17.2.3</b>	<b>Thermoelectric Converters Modeling.....</b>	<b>503</b>	
<b>17.2.4</b>	<b>Thermoelectric Energy Scavenging Microsystem .....</b>	<b>503</b>	
<b>17.2.5</b>	<b>Voltage Converters.....</b>	<b>504</b>	
<b>17.3</b>	<b>Deposition and Characterization Technology .....</b>	<b>505</b>	
	<b>17.3.1</b>	<b>Measurement System of the Thermoelectric Properties .....</b>	<b>505</b>
	<b>17.3.2</b>	<b>Thin-Film Deposition Technology.....</b>	<b>508</b>
	<b>17.3.3</b>	<b>Thermoelectric Thin Films by Co-Evaporation .....</b>	<b>513</b>
	<b>17.3.4</b>	<b>Device Patterning Techniques.....</b>	<b>515</b>
<b>17.4</b>	<b>Thermoelectric Thin Films by Co-Evaporation .....</b>	<b>518</b>	
	<b>17.4.1</b>	<b>N-Type Thermoelectric Thin Films Made of Bismuth Telluride .....</b>	<b>519</b>
	<b>17.4.2</b>	<b>P-Type Thermoelectric Thin Films Made of Bismuth Telluride .....</b>	<b>519</b>
	<b>17.4.3</b>	<b>Thermoelectric Devices .....</b>	<b>519</b>
	<b>17.4.4</b>	<b>Why Scanning Probe? .....</b>	<b>520</b>
	<b>References</b>	<b>525</b>	
<b>18</b>	<b>Evaluation of the Nanoimprinting Process Using Scanning Probe Microscopy (SPM) .....</b>	<b>529</b>	
	Makoto Okada and Shinji Matsui		
<b>18.1</b>	<b>Introduction .....</b>	<b>529</b>	
<b>18.2</b>	<b>Use of SPM to Characterize an Antisticking Layer and a UV-Curable Resin .....</b>	<b>530</b>	
<b>18.3</b>	<b>Evaluation of an Antisticking Layer by SPM .....</b>	<b>532</b>	
	<b>18.3.1</b>	<b>Evaluation of the Fluorinated Self-Assembled Monolayer (F-SAM) Antisticking Layer .....</b>	<b>533</b>
	<b>18.3.2</b>	<b>Evaluation of a Thin Polydimethylsiloxane (PDMS) Layer .....</b>	<b>535</b>

# **Chapter 16**

## **Bridging Nano- and Microtribology in Mechanical and Biomolecular Layers**

**Agnieszka Tomala, Hakan Göçerler, and Ille C. Gebeshuber**

**Abstract** The physical and chemical composition of surfaces determine various important properties of solids such as corrosion rates, adhesive properties, frictional properties, catalytic activity, wettability, contact potential and – finally and most importantly – failure mechanisms. Very thin, weak layers (of man-made and biological origin) on much harder substrates that reduce friction are the focus of the micro- and nanotribological investigations presented in this chapter.

Biomolecular layers fulfil various functions in organs of the human body. Examples comprise the skin that provides a protective physical barrier between the body and the environment, preventing unwanted inward and outward passage of water and electrolytes, reducing penetration by destructive chemicals, arresting the penetration of microorganisms and external antigens and absorbing radiation from the sun, or the epithelium of the cornea that blocks the passage of foreign material, such as dust, water and bacteria, into the eye and that contributes to the lubrication layer that ensures smooth movement of the eyelids over the eyeballs.

Monomolecular thin films, additive-derived reaction layers and hard coatings are widely used to tailor tribological properties of surfaces. Nanotribological investigations on these substrates can reveal novel properties regarding the orientation of chemisorbed additive layers, development of rubbing films with time and the relation of frictional properties to surface characteristics in diamond coatings.

Depending on the questions to be answered with the tribological research, various micro- and nanotribological measurement methods are applied, including scanning probe microscopy (AFM, FFM), scanning electron microscopy, microtribometer investigations, angle-resolved photoelectron spectroscopy and optical microscopy. Thoughts on the feasibility of a unified approach to energy-dissipating systems and how it might be reached (touching upon new ways of scientific publishing, dealing with over-information regarding the literature and the importance of specialists as well as generalists in tribology) conclude this chapter.

## 16.1 Introduction to Nanotribology and Microtribology

Micro- and nanotribology involve studies of friction and wear processes ranging from microscopic to atomic levels. In this section, experimental studies in the field of nano-/microtribology requiring applications with scanning probe microscopy, electron scanning techniques and microtribometers are investigated. Micro- and nanotribological tests presented in this section would be useful to better understand how mechanical and biological layers behave under shearing stress.

Even though atomic force microscopy (AFM) can be operated in the wearless regime, it is also possible to operate the instrument at higher loads for friction studies (e.g. friction vs. load plots) as well as for scratch/wear and indentation studies. These types of operation modules allow the probing of the elastic/plastic response of mechanical and biological films and are the focus of this chapter. Angle-resolved X-ray photoelectron spectroscopy (AR-XPS) helps to understand adsorption mechanisms of molecules on surfaces. At most solid–solid interfaces, the contact occurs in numerous asperities.

Bowden and Tabor's solid/solid adhesion model explains Amonton's friction law on the basis of the small real contact area  $A_c$  which is proportional to the applied load and independent of the geometrical area. Since the friction is proportional to the contact area  $A_c$ , friction is proportional to the load  $L$ . However, the described model is relevant for plastic deformation of asperities. In practice, the applied load is also supported by elastic deformation of asperities. Archard (1957) and subsequently Greenwood and Williamson (1966) confirmed that even for elastic asperity deformation, a statistically distributed, rough surface will result in  $A_c \sim L$  [1]:

$$\mu = \tau_f/H \quad (16.1)$$

When asperities adhere and a shearing force is applied, the junctions can grow plastically since both the normal force and the shear force will couple to produce deformation. This will result in an increase in real contact area and thus in friction coefficient [2]. Tabor used this thought to extend his simple model to

$$\mu = \frac{1}{\delta^{1/2}(f^{-2} - 1)^{1/2}} \quad (16.2)$$

where  $f = \tau_f/p_y$  is the ratio of the shear strength of the film to the yield stress of the bulk deformation material, and  $\delta$  is a constant with value of  $\approx 9$  (assuming that hardness equals three times the yield stress).

This means that Amonton's law of friction results from adhesion of plastically deformed asperities (Tabor's theory), even if also elastic deformation occurs. The ratio of the interfacial shear strength  $\tau_f$  to solid yield strength or hardness is a crucial parameter in determining adhesive friction. To obtain a low adhesive friction coefficient between rubbing rough surfaces in contact, one needs low surface shear strength  $\tau_f$  and/or high hardness  $H$ . These requirements are incompatible for clean

metals but can be met if a thin low shear strength layer is formed on a hard metal substrate. Such a layer has to be thin enough not to bend significantly and thereby increase  $A_c$ .

This concept, namely, using a very thin, weak layer on a much harder substrate to reduce friction is the basis of boundary lubrication and will be used throughout this chapter. Clearly, the state of the surface, for example, adsorbates, the differences of materials in contact and lubricants can greatly affect the interaction and in consequence the friction process.

The tribological mechanical layers and the biotribological biomolecular layers investigated in this chapter serve as protective material of substrates from different environmental conditions.

Chemisorbed layers of ethanolamines (corrosion inhibitors) are the typical examples of adsorbed monomolecular thin films treated in this chapter. The tribochemically additive-derived reaction layer example is triofilm from zinc dialkyldithiophosphates (ZnDDP). Other examples are hard coatings deposited by chemical or physical vapour deposition.

### **16.1.1 Monomolecular Thin Films**

Boundary films can be formed by several processes: physisorption, chemisorption and chemical reactions [3]. In the case of physisorption, no exchange of electrons takes place between the lubricant molecule and the surface – this process involves weak van der Waals forces. Chemisorption means the sharing of electrons and electron interchange between chemisorbed species and the solid surface, resulting in the formation of chemical bonds. Finally, chemical reactions comprise the formation of surface layers with considerable chemical alteration of both additive and surface. The stability and durability of surface films (Fig. 16.1) decrease in the following order: chemical reaction layers (thick films), chemisorbed films (with monomolecular thickness) and physisorbed films (monolayers or multilayers) [4].

In this section, the example of a monomolecular thin film will be the chemisorbed film of a corrosion inhibitor: ethanolamine oligomers. Ethanolamines or aminoethanols are known as multidentate ligands with the possibility to form chelates with metals via their amino, hydroxyl and deprotonated hydroxyl groups. The total formula of these water-soluble compounds is  $\text{NH}_3-n\text{R}_n$  ( $R = \text{CH}_2\text{CH}_2\text{OH}, n = 1 - 3$ ). Ethanolamines are widely used as cleaning agents. In the field of lubrication, they are utilized as anti-corrosion additives, for example, in metalworking fluids.

Chemisorbed layers of the ethanolamine oligomers were studied with AFM and AR-XPS methods to investigate their lubrication properties in the nanoscale. Therefore, the ethanolamines were dissolved in double distilled water. Copper-sputtered silicon wafers served as substrates.

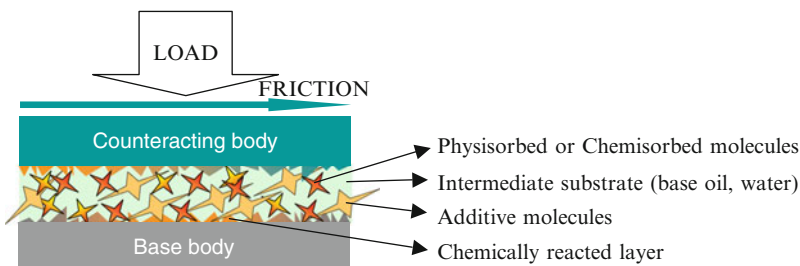


Fig. 16.1 Scheme of interacting additive molecules between surfaces in tribological contact

### 16.1.2 Additive-Derived Reaction Layers

Commercially available lubricants are formulated products composed of a base oil (mineral or synthetic) and a functional additive package designed to achieve a required performance for a specific application. Zinc dialkyldithiophosphates (ZDDPs) have been widely used in the past decades as additives in engine lubrication oil. ZDDP was initially used as an antioxidant, but its excellent anti-wear properties were quickly recognized. The anti-wear properties of ZDDP additives arise from their ability to chemically interact with rubbing metal surfaces to form a protective layer. It protects the surface under conditions where elastohydrodynamic lubrication breaks down. In order to perform effectively, films of this kind must possess a shear strength that is sufficiently low to ensure that the shear plane resists within the protective layer itself, while being high enough to maintain layer integrity [5].

The thickness and distribution of reaction layers formed by ZDDP additives on lubricated contacts is controlled by several operating parameters, including load, temperature, sliding speed, slide-roll ratio and additive concentration. Measurements of additive-derived layer thickness have been performed using a wide range of techniques, showing that ZDDP forms several hundred monolayers thick layers on rubbing surfaces. X-ray photoelectron spectroscopy (XPS), Auger electron microscopy (AES) and secondary ion mass spectroscopy (SIMS) measured an estimated layer thickness of 50–100 nm [5].

A variety of mechanisms have been proposed for the formation of the ZDDP-derived reaction layers, involving oxidative (by reaction with hydroperoxides or peroxy radicals) [6], catalytic (chemisorption on metal), hydrolytic [7] and thermal [8] decomposition of the ZDDP.

The layers are composed of a mixture of short and long polyphosphates with the presence of sulphides and oxides in the layer bulk. A two-layer structure for the ZDDP-derived reaction layers has also been proposed, where a thin long-chain zinc poly(thio)phosphate layer is superimposed on a thicker short-chain mixed Fe/Zn polyphosphate layer, containing embedded nanocrystallites of ZnO and ZnS [9].

The anti-wear films produced particularly by ZDDP are highly uneven. Sheasby and Nisenholz [10] detected the existence of 20- $\mu\text{m}$ -diameter ‘pads’ of ZDDP-derived anti-wear films by means of SEM. Graham et al. [11] found that ZDDP indeed yielded 10–20- $\mu\text{m}$  pads with flattened tops, elongated in the sliding direction and surrounded by lower smaller pads. They also measure mechanical properties of these pads and found that at the centre of the large pads, indentation modulus values were as high as 209 GPa (compared to 220 GPa for the 52100 steel substrate!). An agglomeration of large long pads of polyphosphate chains perform as sacrificing load-carrying ‘platforms’ [5].

### 16.1.3 Hard Coatings

In the past 50 years, during the industrial revolution, solid tribological materials and coatings have continued to play important roles in many engineering areas mainly because mechanical systems rely on them for high performance, durability and efficiency. Recent developments in deposition technologies have provided the flexibility needed for design and development of multifunctional coatings. The use of thin surface coatings (such as diamond, diamond-like carbon, Molybdenum disulfide, nitrides, carbides and their composites and dopants) affords low friction and long wear life of rolling, rotating or sliding mechanical parts and components in recent years [12]. Application of the thin coatings on solid surfaces ensures that premature failures due to thermal, mechanical or chemical incompatibility are virtually nonexistent. In this field, there are almost unlimited numbers of material combinations, surface parameters and application conditions that one can manipulate to achieve better performance and longer durability.

### 16.1.4 Biomolecular Layers

The special types of biomolecular layers that will be in the interest of this study are epithelial tissues. As the term implies in Greek, with ‘epi’ meaning ‘on, upon’ and ‘theli’ meaning ‘tissue’, this type of tissue is covering connective tissues and therefore is the first layer to experience tribology-related mechanochemical contacts in many applications (Fig. 16.2).

Epithelial tissues are generally classified by the morphology of their cells and the number of layers they are composed of. Epithelial tissue that is only one cell thick is known as simple epithelium. If it is two or more cells thick, it is known as stratified epithelium. However, when larger simple epithelial cells are viewed in cross section with several nuclei appearing at different heights, they can be confused with stratified epithelia. This kind of epithelium is therefore described as ‘pseudostratified’ epithelium [13, 14].

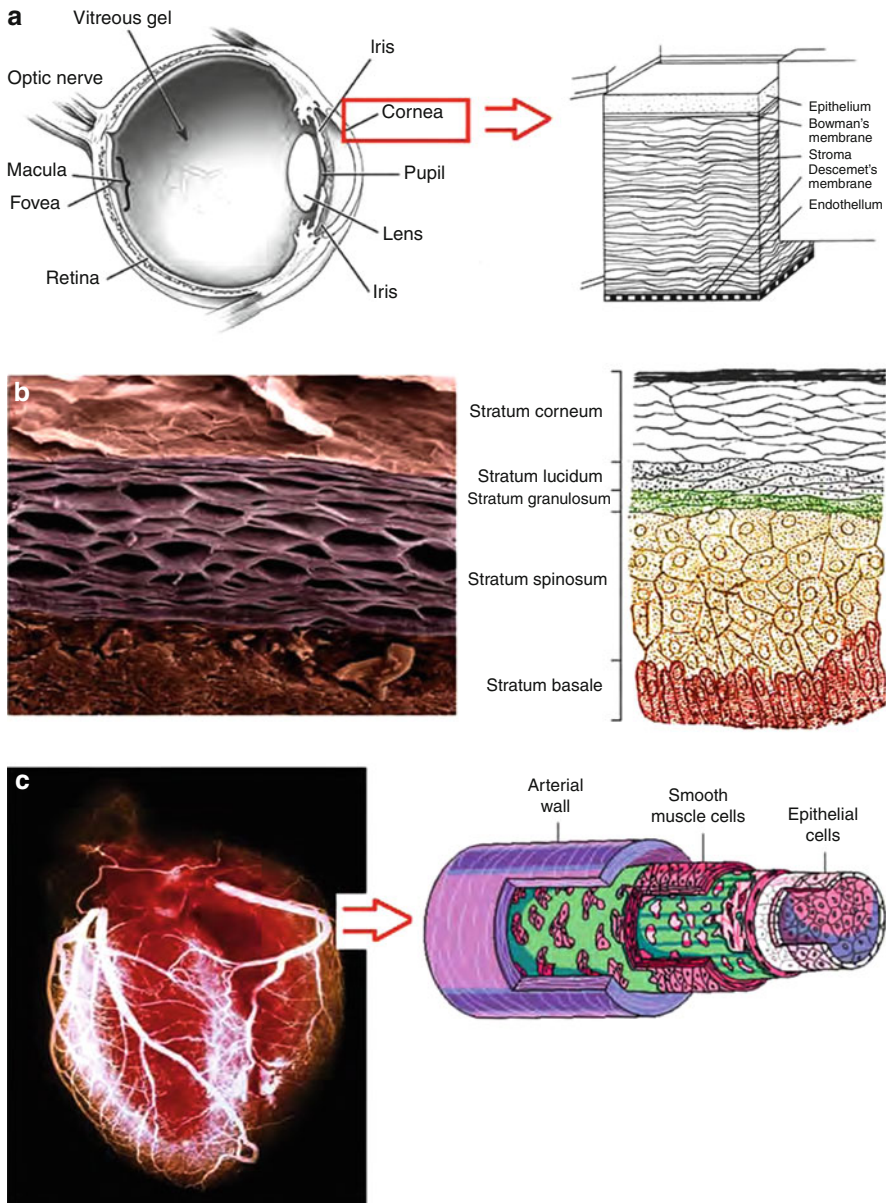


**Fig. 16.2** Different examples of epithelial layers from (a) human eye and the cornea, (b) human skin and stratum corneum and (c) human artery [15, 16]

### 16.1.4.1 Simple Epithelium

Simple epithelium is one cell thick, that is, every cell is in direct contact with the underlying basement membrane. It is generally found in locations of the organisms where absorption and filtration occur. The thinness of the epithelial barrier facilitates these processes.

Simple epithelial tissues are generally classified by the shape of their cells. The four major classes of simple epithelium are squamous, cuboidal, columnar and pseudostratified.

#### Squamous Epithelial Cells

Squamous cells have the appearance of thin, flat plates. They fit closely together in tissues, providing a smooth, low-friction surface over which fluids can move easily. The shape of the nucleus usually corresponds to the cell form and helps one to identify the type of epithelium. Squamous cells tend to have horizontally flattened, elliptical (oval or egg-shaped) nuclei because of the thin flattened form of the cell. Classically, squamous epithelia are found lining surfaces utilizing simple passive diffusion such as the alveolar epithelium in the lungs. Specialized squamous epithelia also form the lining of cavities such as the blood vessels (endothelium) and pericardium (mesothelium) and the major cavities found within the body.

#### Cuboidal Epithelial Cells

As their name implies, cuboidal cells are roughly cuboidal in shape, appearing square in cross section. Each cell has a spherical nucleus in the centre. Cuboidal epithelium is commonly found in secretive or absorptive tissue, for example, the (secretive) exocrine gland the pancreas and the (absorptive) lining of the kidney tubules as well as in the ducts of the glands. They also constitute the germinal epithelium that covers the female ovary.

#### Columnar Epithelial Cells

Columnar epithelial cells are elongated and column-shaped. Their nuclei are elongated and are usually located near the base of the cells. Columnar epithelium forms the lining of the stomach and intestines. Some columnar cells are specialized for sensory reception such as in the nose, ears and the taste buds of the tongue. Goblet cells (unicellular glands) are found between the columnar epithelial cells of the duodenum, the first section of the small intestine in most higher vertebrates. They secrete mucus, which acts as a lubricant.

## Pseudostratified Epithelial Cells

These are simple columnar epithelial cells whose nuclei appear at different heights, giving the misleading (hence ‘pseudo’) impression that the epithelium is stratified when the cells are viewed in cross section. Pseudostratified epithelium can also possess fine hair-like extensions of their apical (luminal) membrane called cilia. In this case, the epithelium is described as ‘ciliated’ pseudostratified epithelium. Cilia are capable of energy-dependent pulsatile beating in a certain direction through interaction of cytoskeletal microtubules and connecting structural proteins and enzymes. The wafting effect produced causes mucus secreted locally by the goblet cells (to lubricate and to trap pathogens and particles) to flow in that direction (typically out of the body). Ciliated epithelium is found in the airways (nose, bronchi) but is also found in the uterus and fallopian tubes of females, where the cilia propel the ovum to the uterus.

### 16.1.4.2 Stratified Epithelium

Stratified epithelium differs from simple epithelium in that it is multilayered. It is therefore found where body linings have to withstand mechanical or chemical insult such that layers can be abraded and lost without exposing subepithelial layers. Cells flatten as the layers become more apical, though in their most basal layers the cells can be squamous, cuboidal or columnar.

Stratified epithelial tissue also differs from simple epithelial tissue in that stratified epithelial tissues do not contain junctional complexes and have their cells bound together only by desmosomes.

Stratified epithelia (of columnar, cuboidal or squamous type) can have the following specializations:

*Keratinized:* In this particular case, the most apical layers (exterior) of cells are dead and lose their nucleus and cytoplasm and instead contain a tough, resistant protein called keratin. This specialization makes the epithelium waterproof, and so is found in the mammalian skin. The lining of the oesophagus is an example of a non-keratinized or ‘moist’ stratified epithelium.

*Transitional:* Transitional epithelium is found in tissues that stretch, and it can appear to be stratified cuboidal when the tissue is not stretched or stratified squamous when the organ is distended and the tissue stretches. It is sometimes called the urothelium since it is almost exclusively found in the bladder, ureters and urethra.

In this chapter, we will focus on the stratified epithelium. Apart from the natural functions of these tissues as reacting and sensing mechanochemical effects in the body and environment, developments in personal care and health-monitoring systems increased the severity and the frequency of the interactions. Human skin is treated not only with mechanical intruders such as razors, shaving machines, epilating systems, heat treatments, laser treatments and clothing produced from

unnatural materials but also chemical intruders such as shaving creams, shampoos, shower gels, perfumes and detergents used to clean clothes that are in contact with the skin. For the people who use contact lenses for medical or aesthetic reasons, the eye is also under the effect of extra force of eyelid and foreign body combined with the hygienic solutions necessary to assure the health of the eye. People who have problems with the arterial or digestive systems may experience arthroscopy or colonoscopy and may have disturbances on the interior walls of the related organs. All these applications show that unlike their natural life cycles and accidental disturbances, epithelial tissues have to respond periodic and more severe insults, sometimes even on daily basis. In this chapter, investigations on human skin stratum corneum (the outermost layer of the epidermis) using atomic force microscopy and the corneal cell lines using microtribotesters will be represented. The suggested techniques are universal and applicable on different cell lines.

## 16.2 Experimental Approach

### 16.2.1 AFM

Micro-/nanotribological studies are needed to develop a fundamental understanding of interfacial phenomena on a small scale. These investigations of interfacial phenomena also involve ultra thin films and micro-/nanostructures – both currently being used in magnetic storage systems, micro-/nanomechanical systems (MEMS/NEMS) and other industrial applications. Probe-based microscopes, for example, the atomic force microscope (AFM), and the surface force apparatus are widely used for such micro-/nanotribological studies [4, 5].

AFM is suitable to study engineering surfaces under dry or wet conditions down to atomic resolution. One of the most notable extensions of AFM imaging capabilities is the possibility to measure lateral forces between the tip and the sample. Thus, the atomic-scale origins of friction can be observed with this technique, usually denoted as lateral or friction force microscopy (LFM or FFM). These possibilities established the AFM as an important tool in the emerging field of nanotribology: the study of the atomic-scale interactions between surfaces in relative motion, such as friction, adhesion, lubrication and wear.

Moreover, the gap between this atomic-scale understanding, microscopic and subsequently macroscopic applications will need to be bridged. Transition from single (nanoscale) asperities to multiple asperity contacts holds the promise to predict tribological behaviour. Much effort has been invested to resolve and quantify tribological phenomena also on nanometre scales.

AFM techniques for quantitative, fundamental nanotribology are in a nascent stage, still some key issues such as force calibration, tip characterization or effects of the environment are neither fully resolved nor standardized.

### 16.2.1.1 Closed Fluid Cell

Part of this work was performed in fluid environment in a closed fluid cell. The fluid cell is a chamber consisting of two halves (Fig. 16.3a) screwed together mechanically: The samples are glued onto glass on the lower part of the closed fluid cell while the upper half basically consists of the electronic interface, the cantilever and a flexible membrane. After screwing together both halves, the fluid cell can be flooded with double distilled water (Fig. 16.3b). Two channels of the cell can be used to inject fluid into the cell and to drain it, respectively. In the next step, the fluid cell is attached to the head of the AFM. After placing the head with the cell onto the moving table, the head is lowered until the cell attaches to the table (Fig. 16.3c). The reference scans in double distilled water environment are carried out when the mounting and calibration procedure of the system is completed. The lateral trace and retrace data are recorded. Then, the additive solutions are injected into the cell with a syringe, and the AFM experiments are performed analogously to the reference measurements.

For reproducibility of the results, it is very important that all parts of the fluid cell have to be properly cleaned (e.g. with isopropanol), and the cantilever and tubes are replaced after every contact with additive solution.

Measurements were performed with an AFM MFP-3D atomic force microscopy (by Asylum Research, Santa Barbara, CA) in a closed fluid cell using non conductive silicon nitride cantilevers with a spring constant  $k = 0.01 \text{ N/m}$  and a resonant frequency  $f_0 = 4\text{--}10 \text{ kHz}$  (Veeco). The main measurement parameters were a scan size of  $5 \times 5 \mu\text{m}^2$  (512 scan points and 512 scan lines), a scan rate of 2 Hz, a scan angle of  $90^\circ$  and a set point of 3.3 nN in contact mode. The recorded data was each trace/retrace of height, deflection and lateral force.

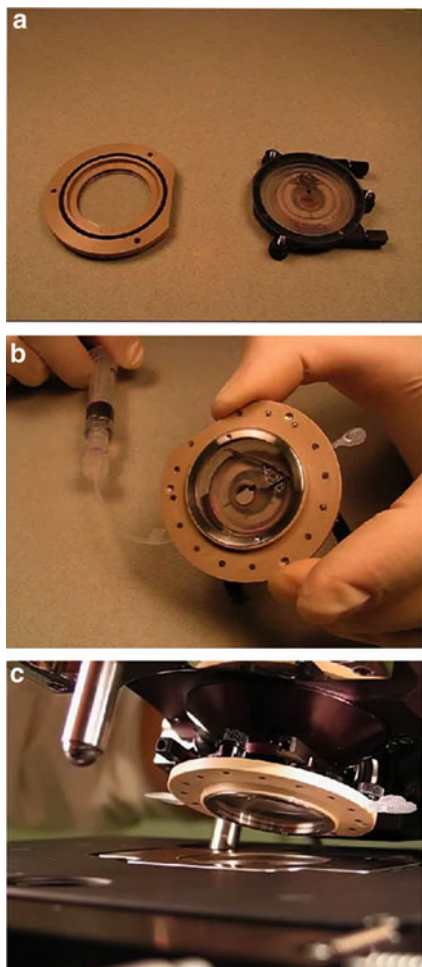
### 16.2.1.2 Friction Measurements

A reliable quantification of the surface morphology based on any AFM lateral image requires determination of the friction coefficient (lateral force dependent on normal forces). However, quantitative determination of friction forces is a challenge, due to difficulties with the calibration of the instrument and cantilever.

Typically, this calibration involves the conversion of the lateral force signal (also named output voltage signal) of the sector area-sensitive photodiode to values of absolute lateral force using (a) the torsional spring constant of the cantilever and (b) the lateral sensitivity of the photodiode. Many existing methods provide calibration approaches with large errors (30–50%) and suffer from poor reproducibility [17, 18].

Bhushan introduced two methods to measure the friction in AFM experiments [19]. For the presented measurements, the lateral force technique has been chosen since it is described as more reliable and objective: The sample is scanned perpendicularly to the long axis of the cantilever beam, to record the lateral force signals in trace and retrace (LT, LRT).

**Fig. 16.3** Assembling the closed fluid cell. (a) Sealing the cell and mounting the appropriate tubes to the four inlet/outlet ports. (b) Filling the cell with fluid and performing a leak test (c) Putting the closed cell assembly onto the head and setting up the tube clamp



this figure will be printed in b/w

Using this arrangement, the friction force between tip and surface will cause the cantilever to twist as soon as the sample moves under the tip. Therefore, the signal intensity between the left and the right detectors will vary as

$$\text{FFM} = \frac{L - R}{L + R} \quad (16.3)$$

where FFM denotes the friction force signal. This signal can be related to the degree of twisting, hence to the magnitude of friction force. By changing the set point parameter in the feedback loop, the normal force applied between probing tip and sample surface can be changed.

The scan area was  $5 \times 5 \mu\text{m}^2$ , consisting of 512 scan lines with each 512 scan points. First, the average values of all 512 lines with 512 points for lateral trace

( $LTV_{avg}$ ) and lateral retrace ( $LRTV_{avg}$ ) from every scan were calculated. To obtain the friction force value (FFV), these two mean values have to be subtracted from each other and divided by two:

$$FFV = \frac{|LTV_{avg} - LRTV_{avg}|}{2} \quad (16.4)$$

The measurements of the friction force values were repeated ten times in every environment (water, water + oligomer) to obtain representative and repeatable results.

Assuming that the friction in the nanoscale follows Amonton's law, the friction force is given by

$$FFV = \mu(SP + F_0) \quad (16.5)$$

where  $\mu$  is the friction coefficient, the set point (SP) is the applied load and  $F_0$  is a force constant. Following the procedure suggested by Beake et al. [20], the force constant is nearly equal to the pull-off force determined from the force–distance curves.

Usually, the FFV and SP values are given in [V] volts as acquired from lateral force measurements.

However, the results can be easily compared with each other because findings in volts are connected with the forces between tip and surface. In order to obtain commonly used units ([N] Newton), the lateral force needs to be calibrated by the determination of the slope of deflection vs. LVDT. The calibration delivers an accurate value of the inverse optical lever sensitivity (*InvOLS*) describing the sensitivity of the detector-cantilever combination. With the knowledge of the accurate value of *InvOLS*, it is possible to calculate FFV and SP in Newton:

$$FFV [V] \times InvOLS [\text{nm/V}] \times \text{spring constant } k [\text{nN/nm}] = FFV[\text{nN}] \quad (16.6)$$

$$SP [V] \times InvOLS [\text{nm/V}] \times \text{spring constant } [nN/nm] = SP [\text{nN}] \quad (16.7)$$

Another solution for calibrating the lateral force signal is the wedge calibration method, introduced by Ogletree et al. [21] and improved after Tocha et al. [22] which gives an error in the calibration factors of about 5%. The ‘wedge’ method of force calibration is an *in situ* method and is applicable for a wide range of cantilevers and materials. This method is based on comparing lateral force signals on surfaces with different well-defined slopes. The known geometrical contribution to the total lateral force gives a different calibration of lateral force response in terms of normal force response. If the normal force constant is known, a quantitative friction measurement can be performed. If it is not known, the ratio of normal to lateral forces (the friction coefficient) can be determined.

An experimental force calibration is performed by sliding the tip across a surface of known slope (grating) and measuring the lateral force signal as a function of applied load. In this work, silicon calibration gratings (MikroMash test structure TGG01, Tallin, Estonia) were used. Such a calibration grating is a 1-D array

of triangular steps having precise linear and angular dimensions defined by the crystallography of silicon (111) planes. The edges of the triangular steps have radii of curvature of less than 10 nm.

Using the wedge calibration method, we experimentally measured the voltage output from the lateral force transducer  $LT_0$ , where  $\alpha LT_0 = LT$  (here the subscript ‘0’ indicates that the value is measured in volts, LT is lateral signal). If we can find  $\alpha$  (Newtons per Volt), we have a direct calibration of the lateral force response to the FFV signal. The calibration constant  $\alpha$  is the product of all the factors of the experiment: the lever lateral force constant, the deflection of the reflected laser as a function of cantilever displacement and the photodiode angular sensitivity.

#### 16.2.1.3 Nano-Wear Tests

Silicon tips on an Aluminium-coated cantilever (OLYMPUS OMCL-HA) were used to perform nanowear tests. The cantilevers were calibrated for topography mode and pull-off force mode using a silicon chip. The value of the spring constant for the silicon tips was 42 N/m. The scan area was  $5 \times 5 \mu\text{m}^2$ . Images were recorded in the contact mode, that is, the feedback electronics and the corresponding software were used to keep the cantilever at constant deflection measuring the sample topography. In order to obtain the maximum LFM signal (torsion motion), the sample was scanned along the direction perpendicular to the cantilever long axis. For each applied force, 512 lateral force loops on an area of  $5 \times 5 \mu\text{m}^2$  were obtained from different regions. For the nanowear measurement, all samples were scratched 40 times using a silicon tip on an aluminium-coated cantilever with a very high spring constant (42 N/m). The load applied to cantilever was 22  $\mu\text{N}$  (equal to a set point of 8 V), the scratching speed was 25  $\mu\text{m/s}$  and the scanning direction was perpendicular to the cantilever long axis and perpendicular to the wear track direction. After the scratching, topography of the scratched area was measured with lower load. The extent of wear was estimated by determining the average depth and width of the scratched area.

#### 16.2.1.4 Colloidal Probes Designed Specifically for *ex vivo* Human Skin Tests

The role of tribology in biomedical and personal care devices is becoming more crucial since it is recognized that the sliding interaction between biomaterials and human tissue is critical for the health and comfort of the patient and the handling performance of these devices. Currently, the tribology of such devices is not well understood, and it is difficult to investigate and optimize frictional properties of the surfaces and materials. The devices operate in a challenging environment that is difficult to simulate: The human tissue surfaces are often very compliant, they respond to mechanical stimulation and the lubrication conditions are variable. Furthermore, existing macroscopic test methods are mostly application-oriented,

this figure will be printed in b/w

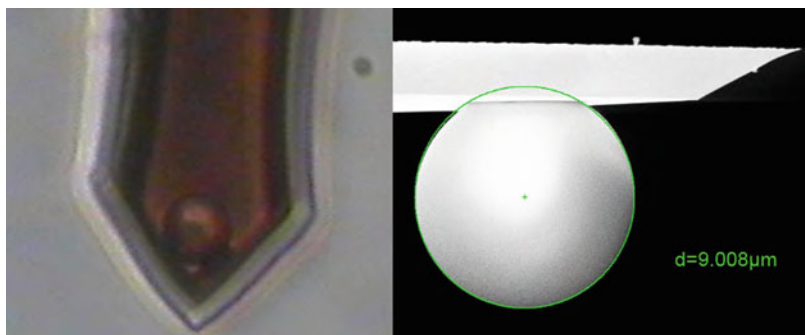


**Fig. 16.4** The colloidal probe

and the results depend on many factors such as handling, environment, operator, test subject, bulk material properties, sample macrogeometry and lubrication conditions. Due to the inconsistency in test results there is a strong need for *in vitro*, microscale lubricity tests to investigate and pre-select surfaces, coatings and materials for medical and personal care devices. The other focus point is the determination of essential mechanical properties of tissues at different scales (cellular level, nano-/micro-/macro-scales) including the response to medical and cosmetic additives.

The aim was to determine the coefficient of friction and adhesive properties of the stratum corneum layer of the human skin, and to identify the microscale distribution of phospholipids, for the correlation to the observed variability of local friction.

The initial step for the research was the production of the colloidal probe for the AFM in order to obtain:

- defined geometry in order to apply models of contact mechanics more accurately,
- increased lateral force sensitivity,
- increase the adhesive interaction between the probe and the skin tissue.

Borosilicate glass microspheres with a diameter of  $10\text{ }\mu\text{m}$  were selected for the application. The main reasons to choose borosilicate were:

- Their roundness is  $>90\%$ .
- Their density is the lowest of most glasses ( $2.2\text{ g/cm}^3$ ).
- They have a very low thermal expansion coefficient ( $32 \times 10^{-7}/^\circ\text{C}$ , for  $30\text{--}300^\circ\text{C}$ ).

Another challenge was the epoxy- and adhesive-free production of the colloidal probe in order to avoid contamination on the human stratum corneum. The possibility of material transfer between the tip and the sample would change the sample-tip interaction by changing the surface energies and also jeopardize the storage conditions standardized for the *ex vivo* biological samples. A novel technique for the production of epoxy- and adhesive-free colloidal probes for atomic force microscopy is reported by Indrieri [23], inspired by the work of Bonaccurso (Fig. 16.4).

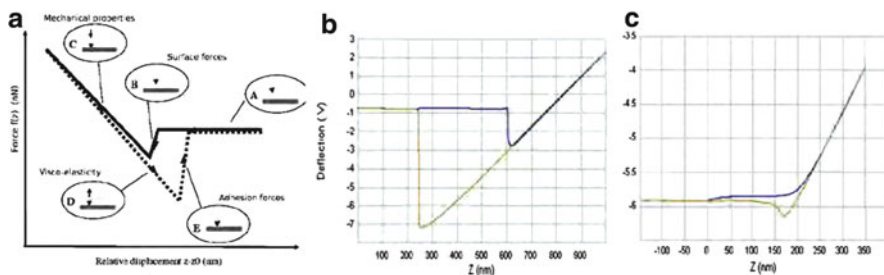


**Fig. 16.5** (a) Typical force curve expected from the interaction of probe and the sample. (b) Adhesion forces observed before contamination. (c) Adhesion forces observed after contamination

Using a cantilever-moving approach, the capillary adhesion between a borosilicate glass microsphere and the AFM cantilever was utilized to attach the sphere to the cantilever free end. A suitable modification of the adhesive properties of the glass substrate makes adhesion of spheres to the substrate weaker than that between sphere and cantilever; this in turn facilitates the detachment of the sphere from the substrate once it has been hooked by the cantilever.

Subsequently, the cantilever-sphere system was cured at 780°C for a few hours to covalently bind the sphere to the cantilever. The procedure is relatively quick and very reliable and produces clean, epoxy-free colloidal probes. The produced probes were characterized with scanning electron microscopy (SEM) and the statistical method of AFM reverse imaging [23].

After three consecutive friction tests conducted in different locations of the stratum corneum, it has been observed that the adhesion forces between the probe and the sample decreased drastically possibly related to the contamination of the probe due to transfer of phospholipids from the skin (Fig. 16.5).

The robustness of the colloidal probe was put to test, and in order to remove contamination, it was subjected to ultraviolet treatment, 15 min of sonication in acetone followed by twice 15 min of sonication in distilled water. The probe was intact after these procedures, no abnormality was observed in functions and expected adhesion forces, observed in force curves from the AFM.

## 16.2.2 AR-XPS

In order to obtain detailed information about the elemental composition, chemical bonds, structure and morphology of a surface, analytical methods such as X-ray photoelectron spectroscopy (XPS) and Auger electron spectroscopy (AES) are favourable candidates. To get in-depth information, depth profiling using ion sputtering is typically used. However, for very thin films (such as monomolecular

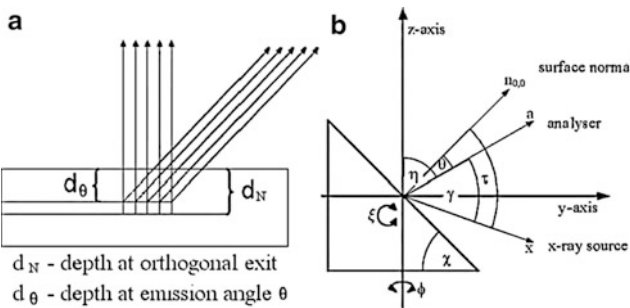


**Fig. 16.6** Geometry of angle-resolved XPS used in calculations. (a) Information depth at normal to the sample surface (orthogonal) and at emission angle  $\theta$  and (b) instrumental and sample geometry used in the AR-XPS measurements

thin films of additives on surfaces), the XPS/AES methodology using sputter depth profiling has got its limitations. Because the ion sputtering process is always accompanied by energy impact, various processes in the analysing region occur, for example, atomic mixing, phase changes or roughening [24, 25].

One way to achieve quantitative results on the near-surface structure of the material is to vary the detection angle in electron spectroscopy for depth-dependent analysis. Due to the finite mean free path of electrons within the solid, the information depth in XPS analysis is of the order of a few nanometres if the electrons are detected at a direction normal to the sample surface. If the electrons are detected at a different angle to the normal, then the information depth is reduced by an amount equal to the cosine of the angle between the surface normal and the analysis direction (emission angle), as shown in Fig. 16.6a. This is the basis for the powerful analysis technique angle-resolved XPS (AR-XPS). The instrument geometry of angle-resolved XPS for the microlab instrument MKII is shown in Fig. 16.6b. In the figure, the emission angle  $\theta$  refers to the angle between surface normal and analyser. In the geometry of our spectrometer, the angle  $\eta$  between the z-axis and the analyser is  $60^\circ$ , and the angle  $\gamma$  between the X-ray source and the analyser is also  $60^\circ$ . The sample holder has a slant angle  $\chi$  equal to  $45^\circ$ .

The stage in the analysis chamber can be moved in  $x$ -,  $y$ - and  $z$ -directions. Additionally, the sample can be tilted and rotated. Before the AR-XPS experiments the stage was positioned in such a way that the analyser axis was pointing directly at the centre of the samples (as shown in Fig. 16.6b).

For AR-XPS measurements in our spectrometer, the emission angle  $\theta$  was varied by rotating the sample around the  $z$ -axis by two revolutions of a step motor controller that corresponds to rotations over an angle of  $20^\circ$ . For the measurements taken at rotation angles  $0^\circ$ ,  $20^\circ$ ,  $40^\circ$ ,  $60^\circ$  and  $80^\circ$ , the corresponding emission angles calculated for geometry of our spectrometer in these experiments were  $15^\circ$ ,  $22^\circ$ ,  $35^\circ$ ,  $49^\circ$  and  $63^\circ$ .

this figure will be printed in b/w

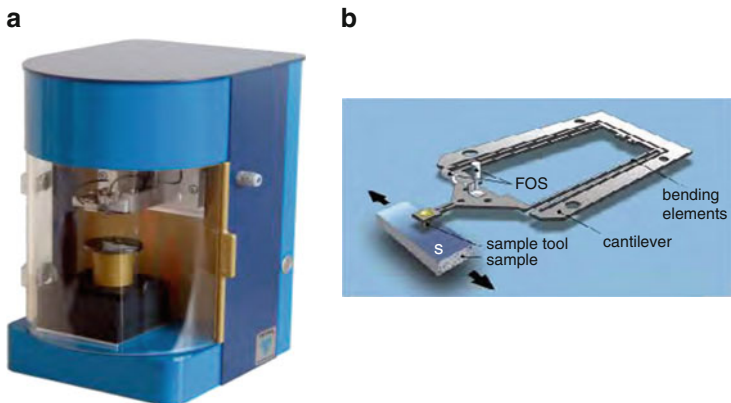


**Fig. 16.7** (a) General appearance of the Falex MUST MTT. (b) Details of the force transducer

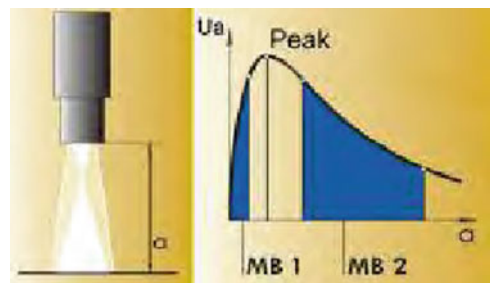
### 16.2.3 Microtribometer

A Falex MUST microtribotester (MTT) was used for the measurements on the corneal cell cultures in order to evaluate/rank lens designs and materials, develop a basic understanding of damage mechanisms, reduce epithelial damage via lens design and determine influencing parameters of the interaction between the eyeball-contact lens-eyelid system such as material composition, material stiffness, friction coefficient, lubrication conditions (buffer solution), normal pressure, shear stress, contact area and sliding speed.

The device operates in a challenging environment that is difficult to simulate: The human tissue surfaces are often very compliant, they respond to mechanical stimulation and the lubrication conditions are variable. Furthermore, existing macroscopic test methods are mostly application-oriented and the results depend on many factors such as the handling, environment, operator, test subject, bulk material properties, sample macrogeometry and the lubrication conditions. Due to the inconsistency in test results, there is a strong need for *in vitro*, microscale lubricity tests to investigate and preselect surfaces, coatings and materials for medical and personal care devices. But the major objective would be to develop a platform that is not only for corneal epithelium for contact lens application but also using cell cultures of different human tissues, for example, vascular endothelium for cardiovascular applications or columnar endothelium for intestinal applications.

The basic functional components of the Falex MUST are a 2-D micro force transducer and various precision motion modules (Fig. 16.7). Relative movements can therefore be carried between a microtool and a probe under control of the power changing effects. The two basic tests, reciprocating or pin-on-disc, are practicable for the applications in microtribology. For our applications, we use the reciprocating mode of the device.

**Fig. 16.8** Characteristic line of fibre optic sensor



#### 16.2.3.1 Operational Principle of the Force Transducer

The force transducer consists of a cantilever (based on a parallel spring system), two mirrors fixed on the moving part of the cantilever and a mechanical support. The geometric dimension of the cantilevers is so that the normal force  $F_N$  and the tangential force  $F_T$  according to the measuring task are optimally coordinated. The cantilever is fixed in a mechanical carrier. With the help of the carrier the force transducer can be changed in the measurement module. Two micromirrors (orthogonal to each other) are used for the fibre optic sensors as reflective surfaces.

#### 16.2.3.2 Operational Principle of the Fibre Optic Sensor

For the measurement of the deflection of the force transducer and the positioning of the piezo drives, fibre optic sensors (FOS) are used. In the tip of the FOS glass fibre bundles are joined and finished to an optical flat. The light radiated from a light conductor bundle (transmission light conductor) is taken up to reflection at a mirror by a further light conductor bundle (reception light conductor) and converted by optoelectronic transducers to electrical signals. The variable projection of the light bundle on the fibres influences the light-induced current.

The process of the sensing rate characteristic  $U_a = f(a)$  is determined by the optical behaviour and the photometric distance law. A characteristic of the sensor consists that it can be operated in two measuring ranges. In the first measuring range (*MB1*, near range), a very distinct rise occurs with a relatively small change in distance. In the second measuring section (*MB2*, far range), the measuring range is larger and the related rise smaller. The maximum of the characteristic is called optical peak. The FOS is calibrated by the manufacturer (Fig. 16.8).

#### 16.2.3.3 Working in Liquid Environment and Tare Values

The difficulty of working in liquid environment has been mentioned before, especially when using devices that are not specifically designed for that purpose. One of the challenges during the work with the Falex MUST MTT was the relatively

small issue that the lifting force of the liquid media during the approach to the surface was not taken into account since the machine was designed to work in dry conditions. The usual operating medium is air (that can be conditioned, thanks to the closed chamber, to different levels of humidity and temperature) for most of the applications with the MTT, so the aforementioned effect on the tare values could be neglected, but since the applications with contact lenses require buffer solutions such as lens solutions or MEM+Glutamax<sup>TM</sup>-1 with high viscosity levels, this effect for our tests could not be neglected.

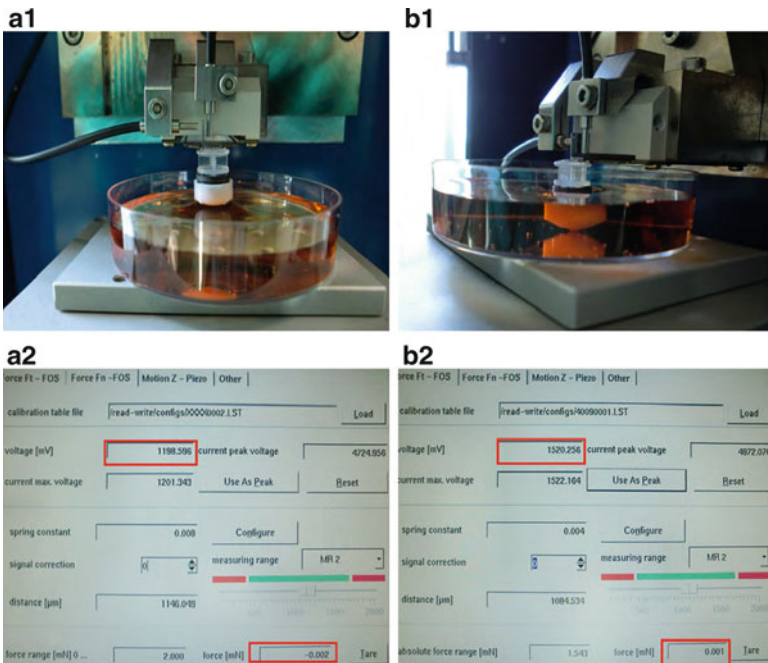
During the calibration of the MTT, it was observed that even though the voltage values given by the internal software change from 1198.596 to 1520.256 mV, the value of the tare forces remained relatively constant (Fig. 16.9). The device eventually gave an error message that the spring reached its maximum displacement even though there was an obvious distance to the bottom surface of the petri dish (Fig. 16.10). The explanation for the error can be found in the concept of tare forces. For each step that the probe automatically approaches the surface, a resisting force is applied by the buffer solution against the probe. This lifting effect of the liquid medium is not stored as the actual tare value and nullified after each step so when the cumulative of these forces equals the target value of the system, the device starts the tests. If the system is handled manually, these forces may equal the maximum force that the spring can support, and then, the system stops the test and retracts the probe.

$$\left. \begin{array}{l} d_1 \rightarrow F_1 \\ d_2 \rightarrow F_2 \\ \vdots \\ \dots \\ d_n \rightarrow F_n \end{array} \right\} F_1 + F_2 \dots + F_n = F_t \rightarrow \text{Start Test} \quad d_T \rightarrow F_T = k_{\text{spring}} \times (\Delta X_{\text{limit}})_{\text{spring}} \rightarrow \text{Stop Test.} \dots d_T : \text{single continuous displacement} \\ \text{Automatic Mode} \qquad \qquad \qquad \text{Manual Mode}$$

This issue was solved by a software update from Falex Tribology that nullifies the tare values after each step of approach. Note that research on biological samples that requires the application of normal forces in the ranges less than a millinewton is sensitive to the natural reactive or surface forces such as lifting forces or meniscus forces. In this case, the weight and the surface area of the probe, approaching velocities and inter-material affinities would play a significant role in the experiment and the parameters need to be revised thoroughly.

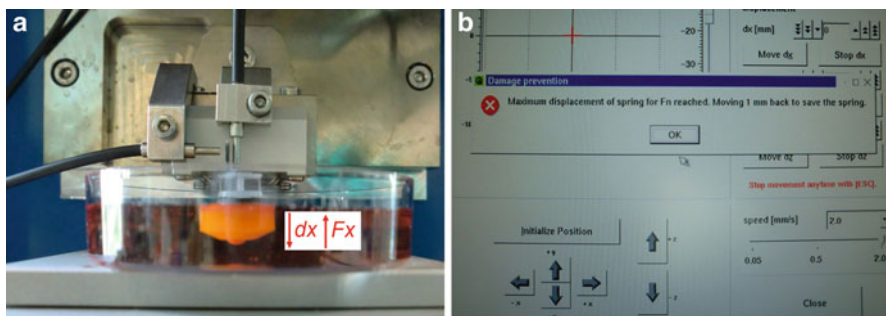
#### 16.2.3.4 Probe Designs for Tests on Epithelial Tissues and Cell Lines

The test apparatus coupled with the Falex MUST MTT requires not only specific design in order to apply sub-millinewton forces but also works completely submerged in the solutions related to the application in focus such as lens solutions



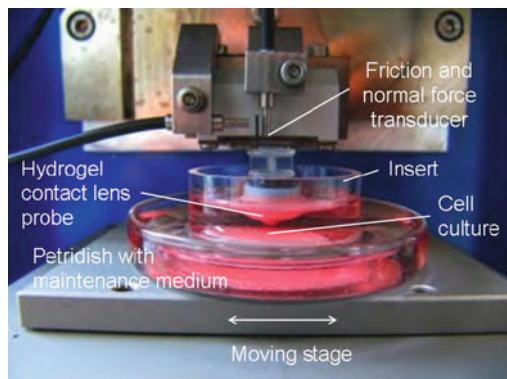
**Fig. 16.9** (a1) Initial contact of the designed probe with the buffer solution surface and the formation of the meniscus. (a2) The related voltage and tare values of a1, screen-captured from the internal software. (b1) The probe at the maximum depth before the actual contact with the petri dish surface. (b2) The related voltage and tare values of b1, screen-captured from the internal software

this figure will be printed in b/w



**Fig. 16.10** (a) The position at which the error message of maximum displacement is given. (b) The error message provided by the MTT

this figure will be printed in b/w

**Fig. 16.11** Experimental setup

for corneal tissue applications or buffer solutions to keep the cell lines in healthy conditions during the tribological tests.

The selection of the appropriate cantilever for the system was the initial step of the probe design. The applications would not only focus on 3-D matrices of stratified epithelial tissues but also on pseudostratified versions of the epithelial cell lines cultured to mimic other organ types of the human body, so the cantilever should be able to apply stable normal forces as low as  $200\text{ }\mu\text{N}$  [50, 51]. For this study, cantilevers with the following specifications were selected:  $k_n = 16\text{ N/m}$ ,  $k_t = 7\text{ N/m}$ ,  $(F_n)_{\max} = 4\text{ mN}$ ,  $(F_t)_{\max} = 3.5\text{ mN}$ ,  $(F_n)_{\min} = 0.04\text{ mN}$  and  $(F_t)_{\min} = 0.0035\text{ mN}$  (resolution). The maximum normal load that was applied to the samples during the study was  $700\text{ }\mu\text{N}$ , and the minimum normal load of  $200\text{ }\mu\text{N}$  with the expected minimum value of COF would result in a minimum friction force value of  $5\text{ }\mu\text{N}$ . In both cases, the selected cantilever would function agreeably for all range of forces in the envisaged application.

The probe needs to be large enough to be completely drawn in the buffer solution in order to eliminate strong effects of meniscus force that could play a critical role in the interaction of the body and the samples. On the other hand, the system should not be so large and lightweight that its self-bending would interfere with the transition of the force from the transducer to the sample, and it should not initiate any crosstalk effect during the test. These two considerations were the driving points that grounded the base of probe design. The final appearance of the probe together with the 3-D tissue construct model can be seen in Fig. 16.11.

Another critical point for the design was the practical mount and dismount of the system without applying any destructive force on the contact lens samples and to avoid any interference that may affect the biological investigation of wear such as dead cells on the contact lens surface. The whole contact lens body was put in the plastic cover and secured by a compliant silicon rubber moulded with a tip of variable diameters (Fig. 16.12a, b). The reason that the tip of the silicon rubber has a defined geometry and shows similarities with the design of the colloidal probe designed for the AFM is to apply models of contact mechanics more accurately

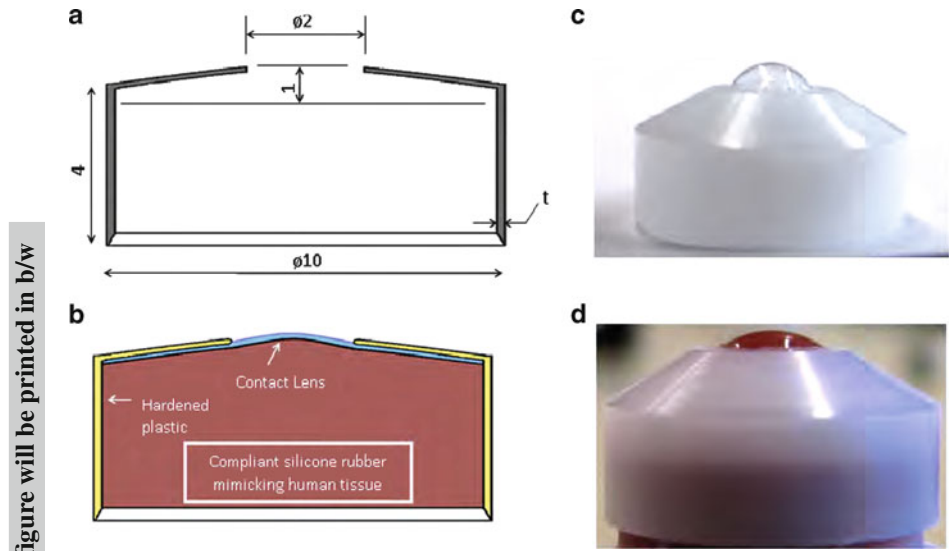


**Fig. 16.12** Details of the hydrogel contact lens probe. (a) Technical drawing of hardened plastic cover. (b) Sketch of final assembly. (c) Photograph of hardened plastic cover and passing form of hydrogel contact lens. (d) Photograph of final assembly

but also to observe the influence of the contact area by means of different mould diameters for future applications. In Fig. 16.12c, it can be seen how the contact lens complies with the supporting silicon rubber. The silicon rubber also has advantages over metal supports, such as mimicking the damping effect of connective tissues supporting the epithelial tissues and making it easier to work in hygienic biological media.

## 16.3 Results and Discussion

### 16.3.1 Monomolecular Thin Films

This section reports on nanoscale tribological investigations on ethanolamine oligomers in aqueous solutions investigated with an AFM closed fluid cell and AR-XPS methods. This work shows oligomer specific lubrication: The most efficient additive reduced friction by 76% with respect to reference friction measurements performed in double distilled water. Further studies with AR-XPS explain the influence of hydroxyl groups and nitrogen-containing ethanolamines on their nanotribological behaviour.

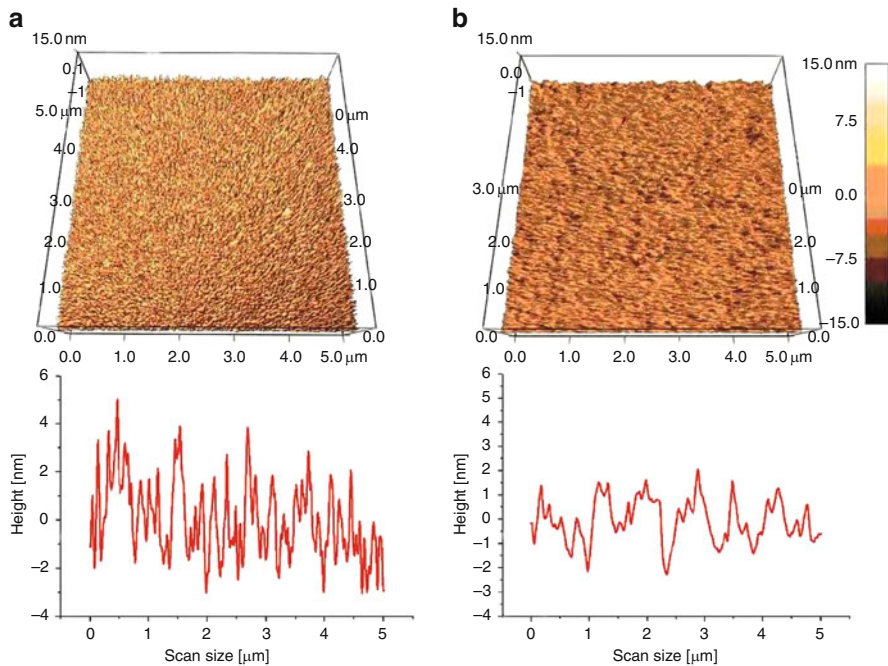


**Fig. 16.13** Topography images. **(a)** Copper sample in double distilled water,  $\text{RMS} = 3.59 \pm 1.97 \text{ nm}$ . **(b)** Copper sample with double distilled water + MEA,  $\text{RMS} = 0.89 \pm 0.58 \text{ nm}$

### 16.3.1.1 Topography

The friction force values and friction coefficient of the virgin surfaces were determined. Then, the additives were introduced into the fluid cell, and the measurements were repeated with the lubricant present [21]. Representative 3-D topography of the ethanolamine monomolecular films is displayed in Fig. 16.13 with section graphs and the root mean square (RMS) parameter.

In the case of ethanolamine film, the surface roughness and RMS parameter were significantly lower compared to pure double distilled water (Fig. 16.13).

### 16.3.1.2 Force–Distance Plots

Force plots are often used to measure the interaction forces between the tip and the surface. This is done by pushing the tip against the surface and then separating the tip and surface. From this data, a number of viscoelastic properties can be studied, such as adhesion, indentation or tribolayer elasticity. There are different force regimes in which forces can be measured with the AFM. Figure 16.14 describes in

this figure will be printed in b/w

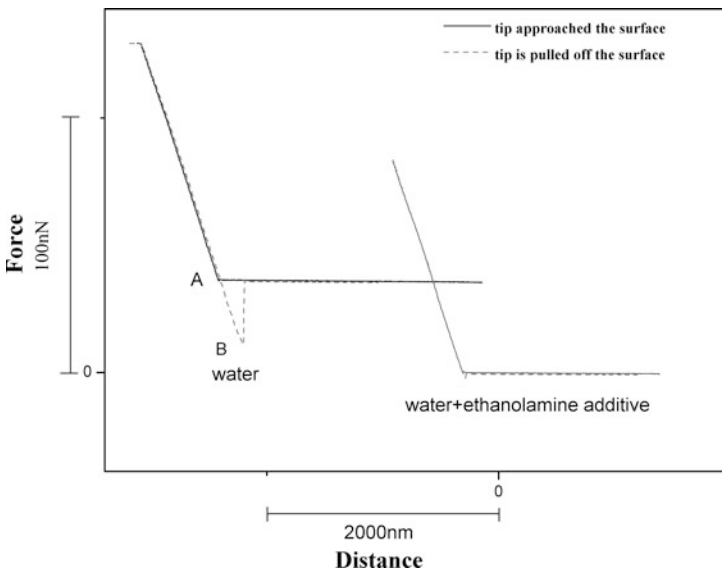


**Fig. 16.14** Force-distance curves of the investigated monolayers

detail the normal force typically experienced by the tip when it is brought towards a sample surface [26].

It can clearly be seen that pull-off forces for double distilled water without any additives are larger than pull-off forces for water with ethanolamines. This fact may be related to an increase of surface energy due to the additives. The hydroxyl groups, being components of ethanolamine oligomers, increase the surface energy, and the increased surface energy in turn increases the pull-off forces.

### 16.3.1.3 Friction Results

The friction force values and friction coefficient of the virgin surfaces were determined. Then, the additives were introduced into the fluid cell, and the measurements were repeated with the lubricant present.

The results show a significant drop in the friction force value after 10 min after introducing ethanolamine oligomer to the solvent (Fig. 16.15).

### 16.3.1.4 Molecular Structure

Orientation of ethanolamine molecules on the steel surface was evaluated using AR-XPS method using ARCTick (angle-resolved XPS spreadsheet) and the SESSA simulation tool (simulation of electron spectra for surface analysis).

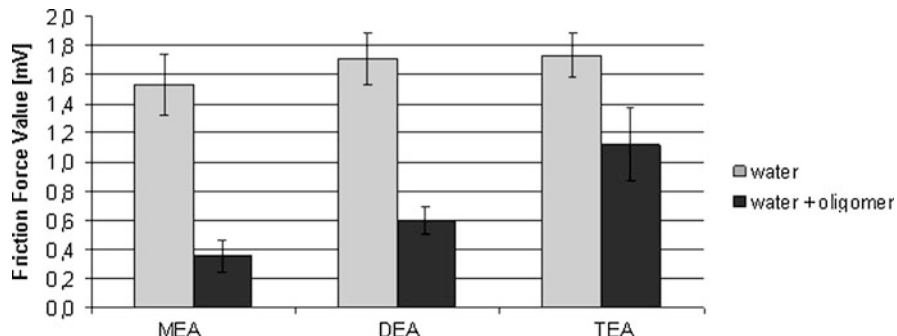


**Fig. 16.15** FFV of double distilled water and decrease of FFV after the addition of solutions with 0.025% ethanolamine oligomer

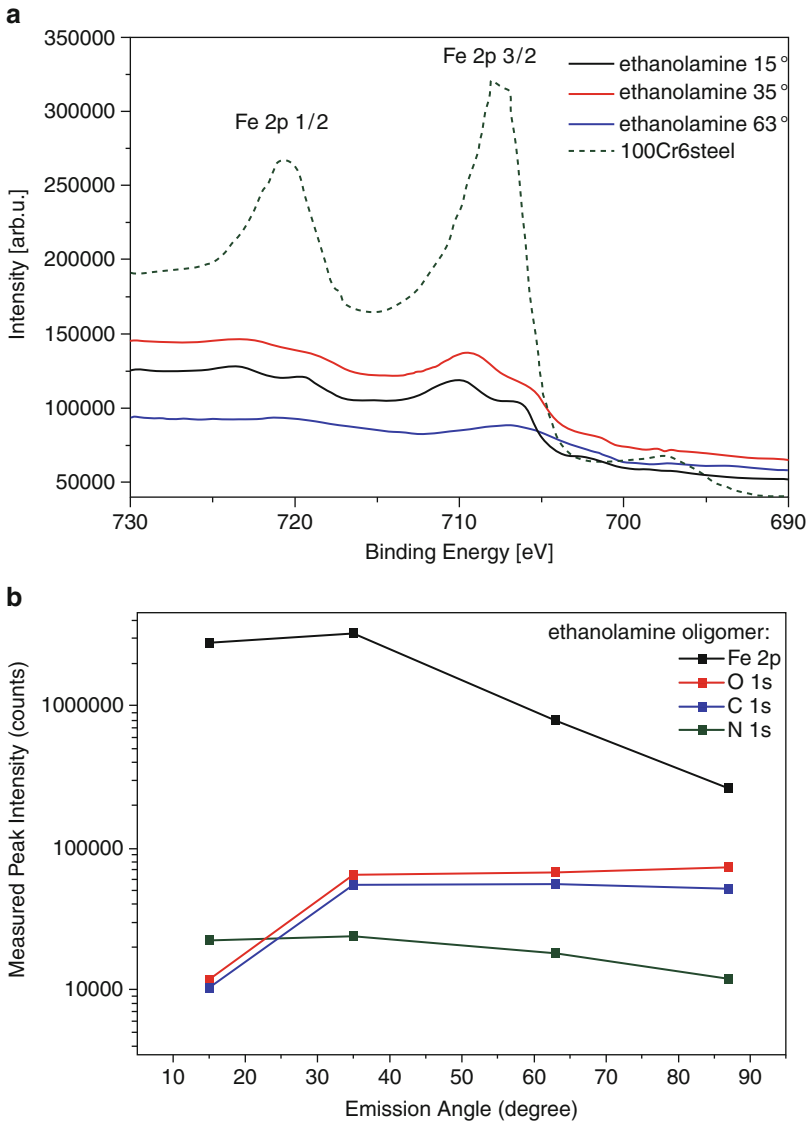
The survey spectra of all steel samples showed only peaks of iron, oxygen, nitrogen and carbon, as expected. The position of photoelectron peaks was determined using Casa XPS, and a combination of Gaussian and Lorentzian peaks was used for fit. The adsorption of ethanolamine oligomers onto a flat steel surface ( $R_a < 5 \text{ nm}$ ) layer takes less than 1 min. The survey spectra show that, after this time, the surface had adsorbed a measurable amount of the oligomers. The quantification of the O1s and C1s peaks showed that there was an equal amount of both oxygen and carbon in the adsorbed films. The C1s peak was in the region typical for alcohols and organic compounds containing nitrogen. The Fe photoelectron region of ethanolamines showed a completely different intensity ratio of the iron and the iron oxide peak (Fig. 16.6a). The loss in intensity of the iron peak was due to the coverage of the surface with the chemisorbed diethanolamine oligomer film. At an emission angle of  $63^\circ$ , the Fe metal peak almost vanished in the spectra recorded from samples with ethanolamine film [27].

Results obtained for ethanolamine clearly reveal the orientation of the molecules on the surface. The intensities of the oxygen peak O1s and the carbon peak C1s increase with increasing analyser angle, and the iron peaks Fe 2p 1/2 and Fe 2p 3/2 and the nitrogen N1s peak decrease with emission angle (Fig. 16.16b). This result indicates that oxygen and carbon were located on top, and iron and nitrogen were beneath. Therefore, it was deduced that the molecules stand upright on the surface, bound to it by the nitrogen atom [27].

Detail analysis of angular-resolved measurements using ARCTick (Fig. 16.17a) and the SESSA simulation tool (Fig. 16.17b) [28] of peaks from Fe, O, C and N confirms our theory that the molecules of ethanolamine oligomer stand upright on the surface, bound to it by the nitrogen atom.

### 16.3.2 Tribocatalytic Additive-Derived Reaction Layer

The formation of a ZDDP-derived reaction layer with rubbing time was studied using a ball-on-disc test rig under mixed rolling-sliding conditions in the boundary lubrication regime. The evolution of the topography and mechanical properties of



this figure will be printed in b/w

**Fig. 16.16** (a) Fe 2p region of monolayers of ethanolamine film on 100Cr6 steel. The spectra are shown for three different electron take-off angles. For comparison, the spectra of clean 100Cr6 steel are marked in a dashed line. (b) Intensity ratio of XPS peaks depending on the emission angle

the layers with rubbing time were studied using AFM. The tribotests were carried out at an applied load of 300 N which resulted in a maximum Hertzian contact pressure of 1.9 GPa (contact diameter 540  $\mu\text{m}$ ) at a slide to roll ratio SRR = -10%. The temperature was set constant at 90°C for all the tests [29].

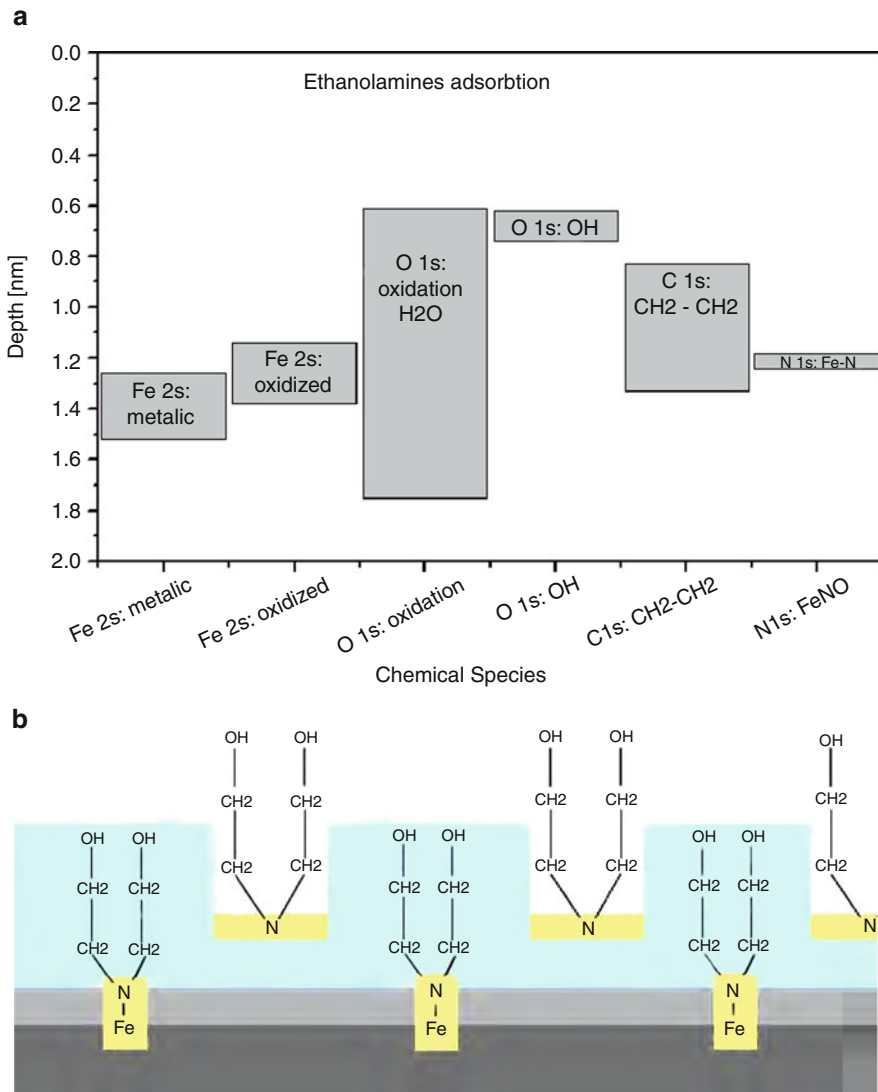


**Fig. 16.17** Proposed mechanism of a chemisorbed monomolecular thin layer of ethanolamine oligomer on a steel surface based on (a) the stratification method with the ARCTick tool and (b) based on the SESSA simulation tool

In order to understand the nature of the interaction between the cantilever tip and the formed reaction layer, deflection displacement curves were recorded. Figure 16.18 shows the deflection of the cantilever tip as a function of the distance from the reaction layer formed in the rubbing steel surfaces. The solid line indicates the tip approach to the surface, while the dashed line represents the tip being pulled away from the surface. The vertical separation between the point where the tip was touching the layer and the point where the tip was pulled away from it together with

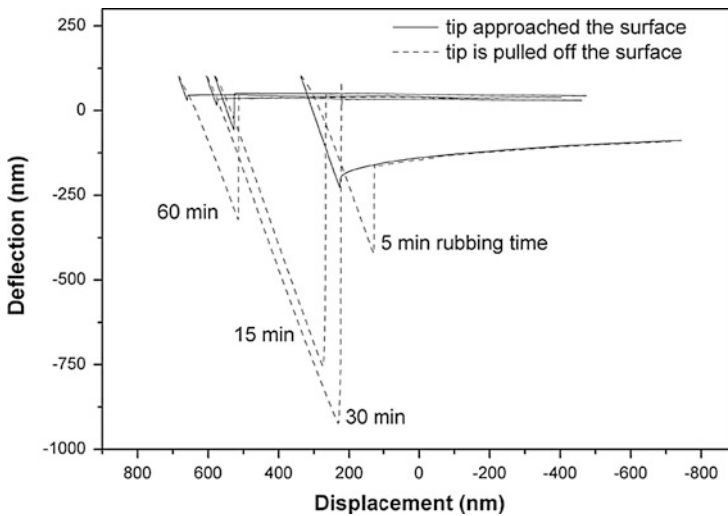


**Fig. 16.18** The deflection of the cantilever tip as a function of the distance from the wear track surface for the investigated samples

the spring constant of the cantilever ( $0.1 \text{ nN/nm}$ ) was used to calculate the pull-off (adhesive) force [4].

Figure 16.18 shows that with increasing ZDDP-derived reaction layer thickness, the force needed to pull off the cantilever from the surface increases. This fact is related to high adhesion and plastic deformation, due to the presence of a soft surface layer formed by ZDDP.

Samples after a 5 min test exhibit a thin reaction layer, the cantilever has alternate contact with asperities from the steel surface and the layer. This results in small pull-off values when the tip engages the elevated asperities and in high lateral force response.

Samples after a 15 min test and after a 30 min test present a thick and soft reaction layer that entirely covers the steel surface. The cantilever interacts only with the soft layer covering the surfaces, resulting in long-distance curves, low friction but high wear volume on the nanoscale. The larger adhesive properties of the soft layer are caused by the molecular interactions between the molecules attached to the tip and the molecules in the layer.

When rubbing progresses further, the additive-derived layer experiences a constant roughening and hardening with rubbing time, as indicated by the nano-wear tests (Fig. 16.19d), which show no indentation for the layer after 1 h rubbing time. These processes may be responsible for the observed increase in friction and wear protection with rubbing time of the additive-derived reaction layers, in both the macro- and the nanoscale.

The 3-D AFM images showing the topographies of the ZDDP-derived layers are illustrated in Fig. 16.19. Section graphs attached to the AFM images show the height

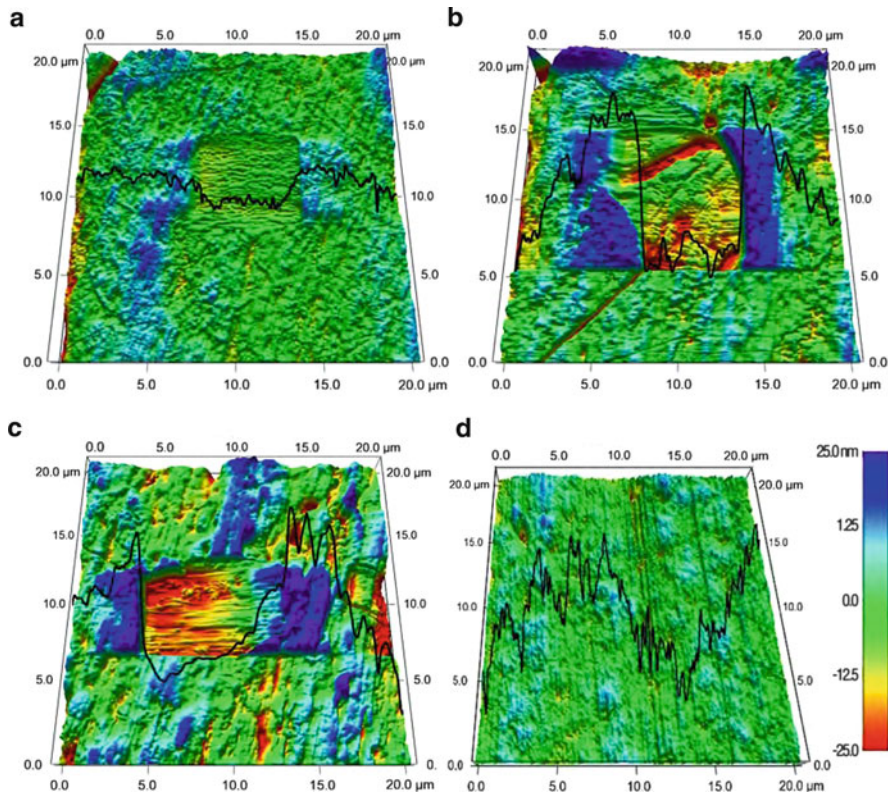


**Fig. 16.19** AFM images showing the  $20 \times 20\text{-}\mu\text{m}^2$  topographies of the investigated samples after nano-wear indentation with horizontal section graph of height distribution. (a) After 5 min ball-on-disc test time, (b) after 15 min, (c) after 30 min and (d) after 60 min

distribution across the scan. Section graphs have the same scale as the colour scale on the right side of the AFM images.

ZDDP reaction layers form only in the rubbing tracks, where actual tribological contact occurs [30]. The reaction layer forms initially as separate patches on the steel surfaces and gradually develops to form a continuous-like structure, as illustrated in Fig. 16.19. A three-stage process can be used to describe the evolution of the layer morphology. In the first stage (Fig. 16.19a, b), the layer growth mechanism begins on micro-asperity contacts at the steel surface, leading to the formation of thin pads. In the second stage as rubbing progresses, the pads continue to grow and coalesce to form a complete layer formed over the surface (Fig. 16.19c). AFM investigations showed that such an additive-derived reaction layer consists of large wear pads, smaller anti-wear pads and lower valleys between the anti-wear pads [11]. In the final stage, the continuous rubbing of the surface causes the disintegration and spreading of the tribolayer to form progressively smaller pads (Fig. 16.19d) [26]. A rough and hard layer develops, reaching a ‘limited thickness’ of approximately 70 nm.

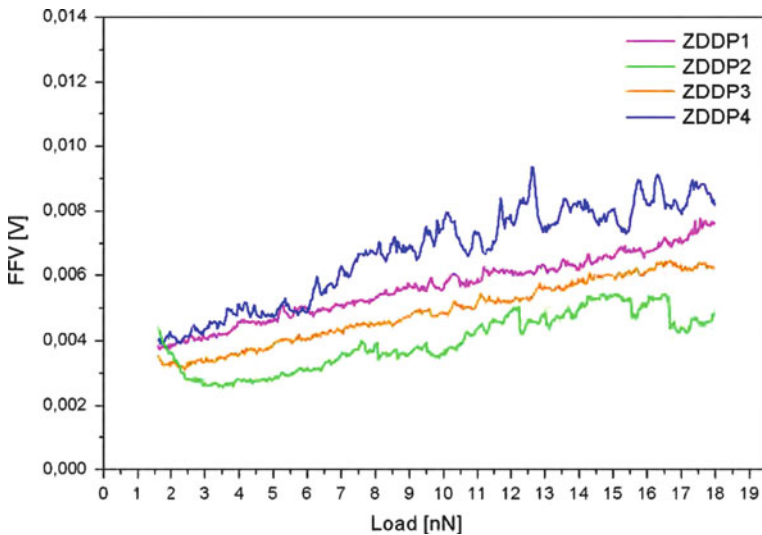


**Fig. 16.20** The variation of friction force as a function of applied load for the investigated samples

Nanowear tests using a cantilever with high spring constant showed that ZDDP-derived layer is initially softer, undergoing a hardening process with rubbing time. The indentation reaches the steel substrate for a sample after 5 min test. The wear depths for samples after 15 and 30 min tests are very similar (between 20 and 30 nm), and despite the uncertainty on the layer base line, none of the indentations reached the substrate. The results obtained for a sample after 1 h test, where no indentation was observed after the nanowear test, indicate a possible hardening process parallel to the roughening process of the layer that has also been observed, with the development of pad-like features [31]. Previous studies [19,32] have shown how those features are higher than the surroundings and present a higher hardness and elastic modulus, which is attributed to the load-carrying capacity of the layer (Fig. 16.20).

### 16.3.3 Hard Coatings

Diamond film is one of the hardest materials and is well known for several extraordinary features such as high mechanical strength [33], excellent thermal conductivity, outstanding wear and friction properties [34], high chemical inertness [35], etc. These films exhibit high surface roughness because of their columnar growth [36], making them unsuitable for many applications such as in microelectronics and as optical components [37]. However, end use tends to favour

this figure will be printed in b/w

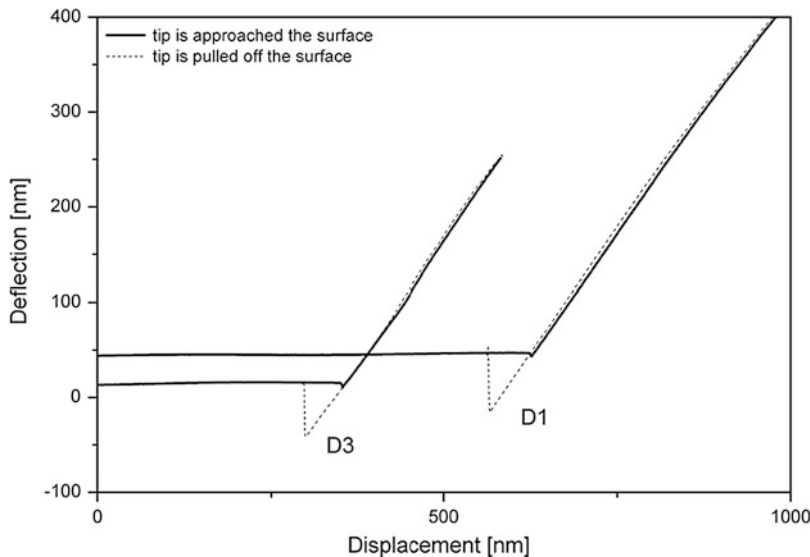


**Fig. 16.21** Force spectroscopy of the investigated diamond films

a particular crystallographic surface texture, purity and thickness matched to the surface that offers the most compatible properties. Thus, properties such as broad optical transparency, high refractive index, wide band gap, low or negative electron affinity, transparency to light from deep ultra violet to far infrared and low thermal expansion make these films suitable for numerous industrial applications [38].

The morphologies of chemical vapour deposited (CVD) diamond films can be changed over a wide range by controlling the process parameters of the deposition. The surface morphologies of the film govern the micro- and nanomechanical properties of the film. In view of these points, diamond film having faceted morphology is presented in this section. It has been deposited using the microwave chemical vapour deposition (MWCVD) technique.

Figure 16.21 shows the deflection of the cantilever tip as a function of the distance from the film surfaces for all two films. In all cases, the darker line indicates the tip approach and the lighter line represents the tip being pulled away. The vertical separation between the point where the tip is touching the film and point where the tip is pulled off the film is a measure of the pull-off (adhesive) force. The product of this horizontal distance of separation and the spring constant of the cantilever ( $0.1 \text{ nN/nm}$ ) gives the pull-off forces [4]. The pull-off forces for two diamond films D1 and D3 are 21.3 and 13.1 nN, respectively. Film D1 represents faceted morphology with mainly  $\text{sp}^3$  bonding, whereas film D3 represents fine ballas morphology with mainly  $\text{sp}^2$  bonding.

this figure will be printed in b/w

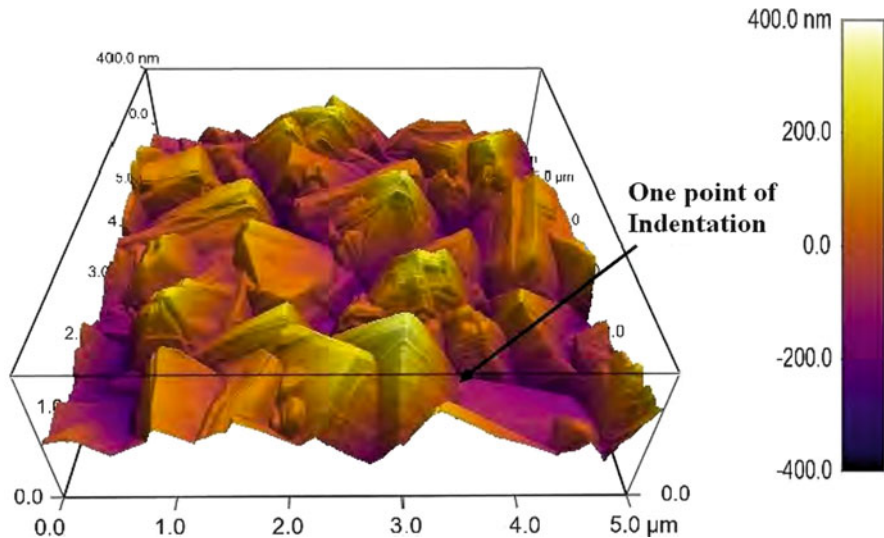


**Fig. 16.22** Topography of the investigated diamond film

The 3-D AFM image showing the topography of the investigated diamond film is given in Fig. 16.22. For the investigated sample, the diamond growth conditions were ‘optimal,’ this results in well-faceted pure diamond crystals with mainly  $sp^3$  bondings.

The influence of the applied load on the friction force is depicted in Fig. 16.23. The friction force decreases with increase of the applied load. This suggests that friction force is not governed by ploughing mechanism since in this case, the friction force would increase with an increase of applied load when ploughing plays important role. Rather, it is controlled by surface force.

### 16.3.4 Biomolecular Layers: Tribological Investigation on Human Stratum Corneum Epidermis Using Atomic Force Microscopy

#### 16.3.4.1 Topography

Forming the interface with a desiccating external environment, the primary function of the stratum corneum is to retard evaporative water loss from the aqueous interior. The stratum corneum also protects against mechanical insults and the ingress of foreign chemicals and microorganisms. It provides the first defence against ultraviolet light, screening out more than 80% of incident ultraviolet *B* irradiation. Taking these considerations into account, stratum corneum epidermis

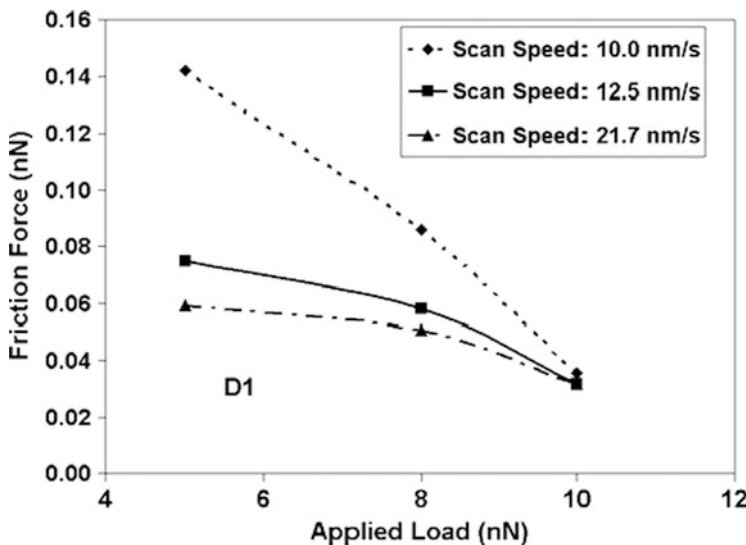


**Fig. 16.23** The influence of applied load on the friction force of the investigated film

can be viewed as a hard coating material, comparable to the ones used in mechanical applications.

Understanding the structure and function of the stratum corneum is vital because it is the key to healthy skin and its associated attractive appearance. During cornification, the process whereby living keratinocytes are transformed into nonliving corneocytes, the cell membrane is replaced by a layer of ceramides that become covalently linked to an envelope of structural proteins (the cornified envelope) [39, 40]. This complex surrounds cells in the stratum corneum and contributes to the skin's barrier function. Corneodesmosomes (modified desmosomes) facilitate cellular adhesion by linking adjacent cells within this epidermal layer. These complexes are degraded by proteases, eventually permitting cells to be shed at the surface. Desquamation (skin peeling) and formation of the cornified envelope are both required for the maintenance of skin homeostasis. A failure to correctly regulate these processes leads to the development of skin disorders [39].

Cells of the stratum corneum contain a dense network of keratin, a protein that helps keep the skin hydrated by preventing water evaporation. These cells can also absorb water, further aiding in hydration and explaining why humans and other animals experience wrinkling of the skin on the fingers and toes ('pruning') when immersed in water for prolonged periods. In addition, this layer is responsible for the 'spring back' or stretchy properties of skin. A weak glutinous protein bond pulls the skin back to its natural shape.

this figure will be printed in b/w

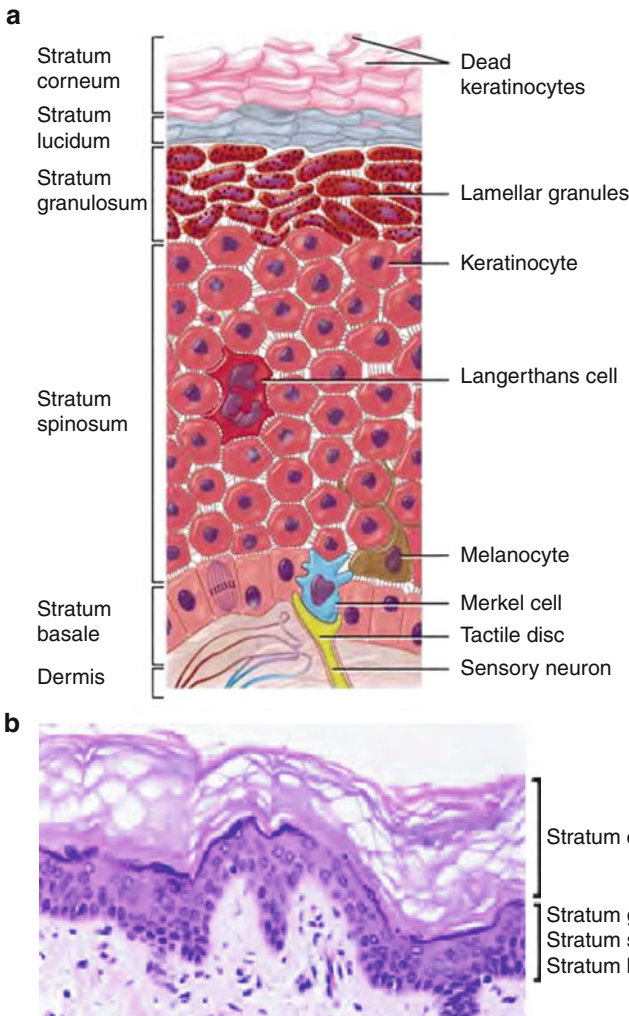


**Fig. 16.24** (a) Layers of the epidermis. (b) Details of the upper three levels of the epidermis [41]

The thickness of the stratum corneum varies throughout the body. In the palms of the hands and the soles of the feet, this layer is typically thicker since these regions require additional protection in order to grasp objects and avoid injury. In general, the stratum corneum contains 15–20 layers of dead cells. The stratum corneum has a thickness between 10 and 40  $\mu\text{m}$  (Fig. 16.24).

Skin samples were obtained from the Department of Pharmacy, University of Milano, after aesthetic surgery following the standards introduced by Blank and McAuliffe [42]. Full-thickness skin was sealed in evacuated plastic bags and frozen at  $-20^\circ\text{C}$  within 24 h of the removal. Prior to the preparation, skin was thawed to

this figure will be printed in b/w

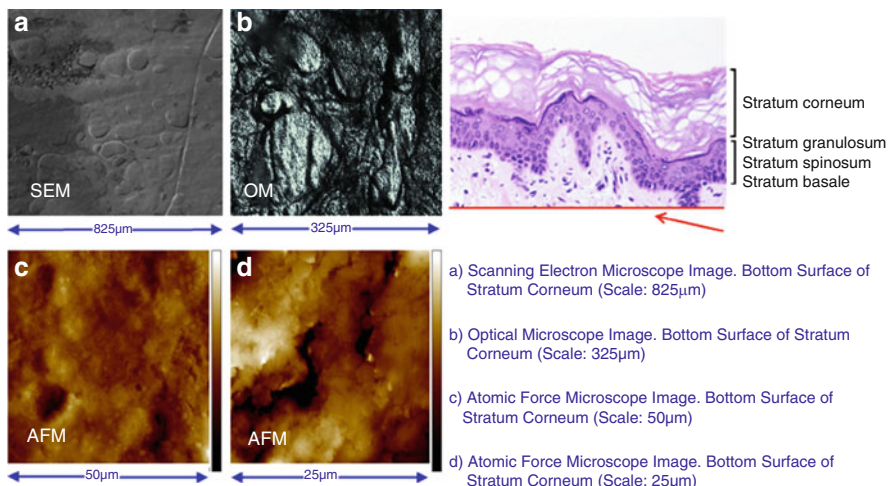


**Fig. 16.25** Bottom view of stratum corneum acquired with different kinds of microscopy

room temperature, and the excess fat was carefully removed. The skin sections were cut into square pieces, and after immersing the skin in water at 60°C for 1 min, the epidermis was gently separated from the remaining tissue with forceps and left to dry. The dried samples were wrapped in Aluminium foil and sealed in plastic bags. When the skin samples were received, they were cut into pieces that are suitable for AFM investigations, and the pieces were put into the freezer at -40°C. Before the measurements, each piece was first thawed in the fridge at -4°C for 2–3 h and then at room temperature for 4 h. No extra procedures such as nitrogen fluxing and cleaning with distilled water were conducted before the measurements.

The initial challenge for the investigation on stratum corneum epidermis was to identify the proper side to conduct the tests. Both sides of stratum corneum, open to the environment and laying over stratum granulosum, show significantly different morphologies. These differences would play a vital role in the tribology-related applications. For this purpose, images of both sides of the skin samples were taken, without any assumptions on the ‘proper side’ beforehand.

In order to understand the morphology of the two sides of the stratum corneum samples, the following imaging techniques were used: SEM, optical microscopy and AFM. The side laying over stratum granulosum shows significant round patterns as the mark patterns of granules that gives the name to the layer (Fig. 16.25). On the other side, the top layer of stratum corneum, laminar patterns can be seen, as expected (Fig. 16.26).

The detailed images gathered by AFM show formations that resemble layers of corneocytes, that is, protein complexes that are made of tiny threads of keratin in an organized matrix (Fig. 16.27).

this figure will be printed in b/w

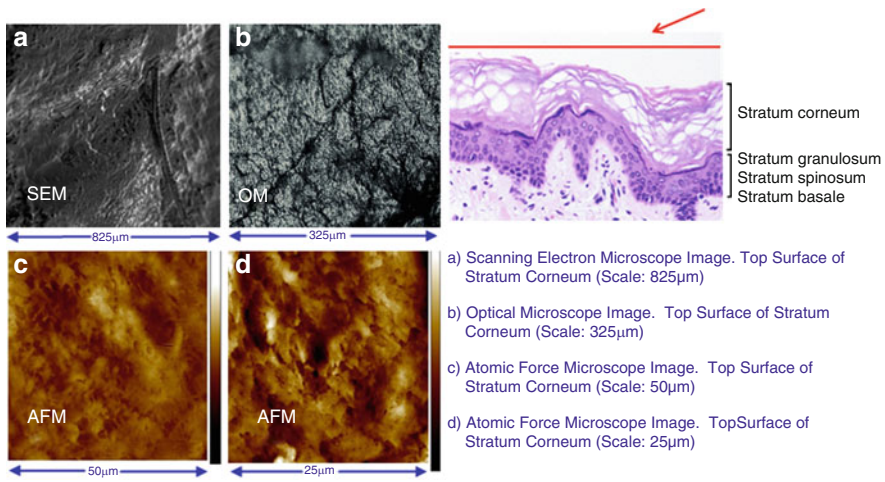


**Fig. 16.26** Top view of stratum corneum acquired with different kinds of microscopy

this figure will be printed in b/w

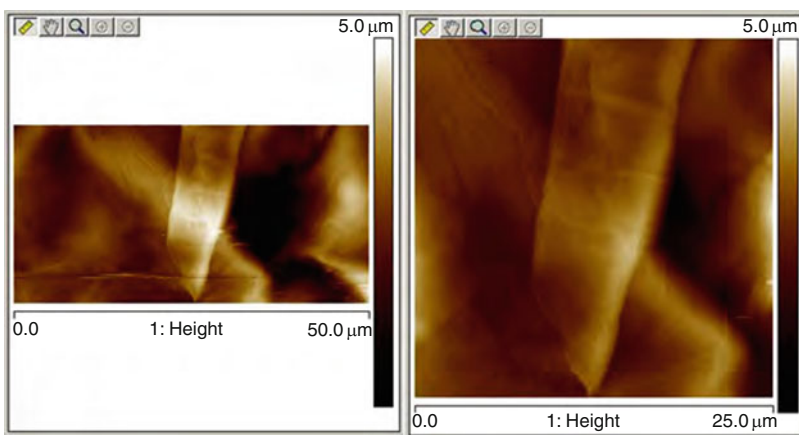


**Fig. 16.27** AFM images with formations that resemble layers of corneocytes

#### 16.3.4.2 Force–Distance Plots

Investigations on the topography of the stratum corneum were conducted using a rectangular tip with the Nanoscope V Bioscope 2 AFM (Veeco Instruments). Following the capture of the topography image, the ‘point and shoot mode’ of the AFM was used in order to investigate the mechanical properties of the stratum corneum epidermis.

‘Point and shoot’ is a new function of the Nanoscope V controller. By this function, force or tunnelling spectroscopy can be precisely located at any XY coordinate in an image, with a single click of the mouse. To operate this function,

this figure will be printed in b/w

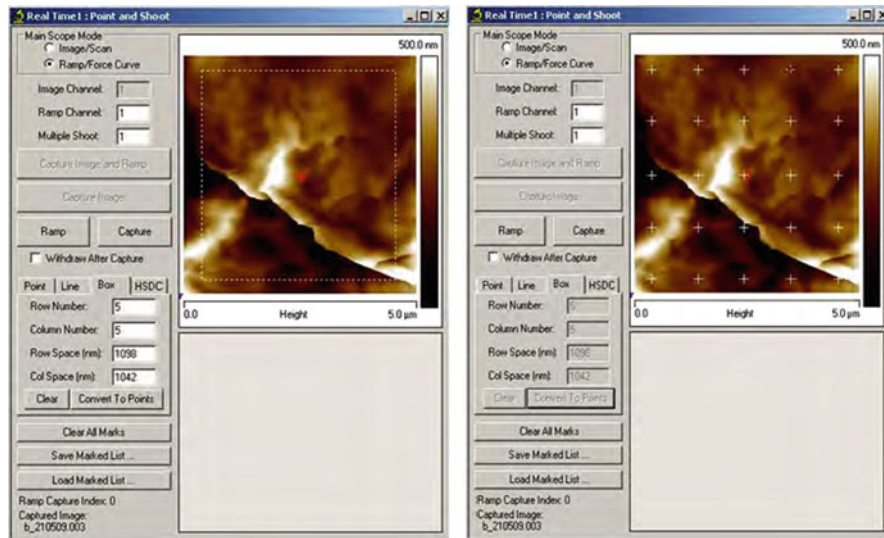


**Fig. 16.28** ‘Point and shoot’ selection on selected area of stratum corneum epidermis

some parameters should be set similar as is done in the normal force mode at the beginning. Then, clicking the mouse at the respective location marks points of interest. The tip ramps simultaneously. In Fig. 16.28, the area of interest for mechanical observation can be seen. Selecting different numbers for columns and rows for the selected area can change the amount of the points, and the AFM stores the force curve information for the selected points on the area. Each point can be selected afterwards to be represented on a scaled diagram to be observed or compared with each other. Two extreme points on the topography map have been carefully chosen to reveal the differences in the force plots (Fig. 16.29).

Significant differences were observed between the dark area and the bright areas. In the dark area, the force curve reaches a plateau that looks as if the force exerted by the probe was damped by a viscous material – this is assumed to be the first sign of phospholipids on the stratum corneum epidermis.

The test was repeated using the force-volume mode of the AFM. Force volume produces a 2-D array of force-distance measurements over a specified area to display images of force variations and topography along with individual force curves at any point.

Any point on the image acquired by AFM (Fig. 16.30) can be chosen for investigation, thanks to the abilities of force-volume mode. By reproducing the preceding point-wise analysis and by scanning the sample surface, a force-volume image  $f(x, y, z)$ <sup>1</sup> is obtained. This image is formed from the collection of force spectra  $f(z)$  on a grid  $(x, y)$  representing the sample surface (Fig. 16.30) [43].

It can be seen that the aforementioned plateau on the force curves related to the selected point on dark area was observed. This shows the postulate is repeatable and

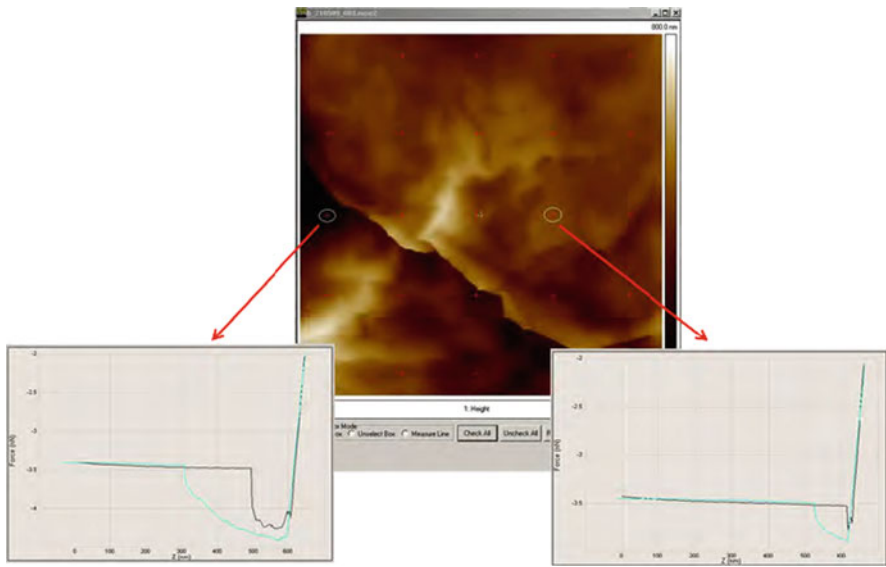


**Fig. 16.29** Force curves stored for two different zones of stratum corneum

is a rational approach to have better understanding of the phospholipid distribution on the stratum corneum epidermis (Fig. 16.31).

The force curves provided by the force-volume test can be interpreted both in the approaching and retracting parts. The analysis of these two parts separately will give us a better understanding of topography and possible distribution of the phospholipid layers (Fig. 16.32).

Finally, the approach was tested one more time, this time not in order to test repeatability but to ensure that the system is navigable when the colloidal probe designed specifically for the friction measurements on the stratum corneum is used (Fig. 16.33).

No reportable issues have been experienced during the acquisition of the topography and lateral force images with the colloidal probe. The force-volume results gave a clear capture of the plateau on the force curve when the point is selected on the dark area (Fig. 16.34).

#### 16.3.4.3 Friction Measurements

AFM is one of the most powerful techniques for the investigation of tribology and, in particular, of nanofriction [44]. An AFM can simultaneously acquire topographic and friction maps of surfaces, operating in the so-called friction force mode, with nanometre resolution. Friction force microscopy (FFM) is possible since the vertical and lateral deflections of the cantilever supporting the AFM tip can be acquired

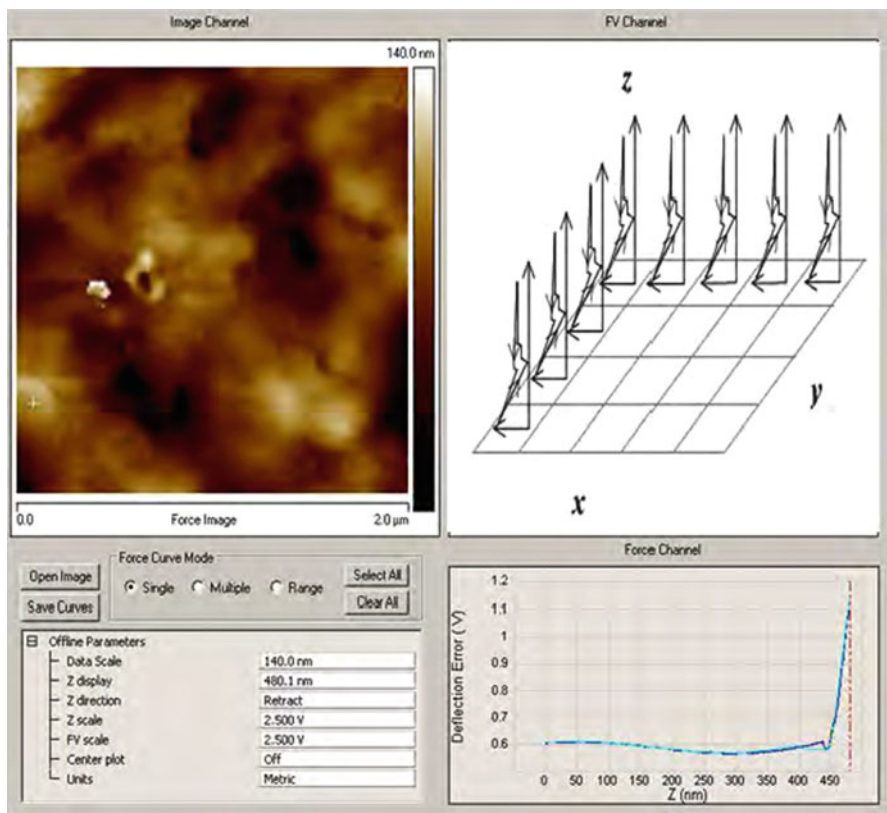


**Fig. 16.30** Data acquired by AFM during force-volume measurements

simultaneously. The former are related to changes in the topography, while the latter are proportional to the friction force between the tip and the sample surface [45].

In order to perform quantitative nanofriction measurements, it is necessary to control and accurately measure both the magnitude and the direction of the forces acting on the AFM tip. However, because of the local tilt of the surface, forces acting on the tip can be different from those inferred using the standard reference frame of the laboratory. The effects of surface topography on nanofriction measurements have been studied, although a general theory is still lacking [46, 47].

Podestà et al. considered the topographic correction and inquired whether it was possible to follow a model-independent approach, providing the friction vs. load characteristics of the system under investigation without the need for postulating any particular contact-friction model [48]. They solved the problem of the topographic correction in the particular case of the adhesive multiasperity contact, which is common in many experimental setups. To this purpose, they introduced a modified version of Amonton's law for friction [49] (linear dependence of friction on load) that should better apply to the case of low loads and few asperities in contact.

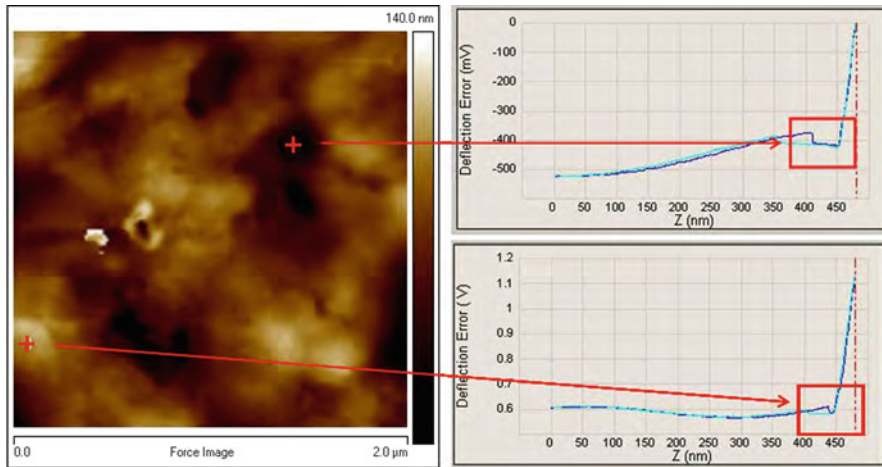


**Fig. 16.31** Selected points on the image acquired during force-volume mode

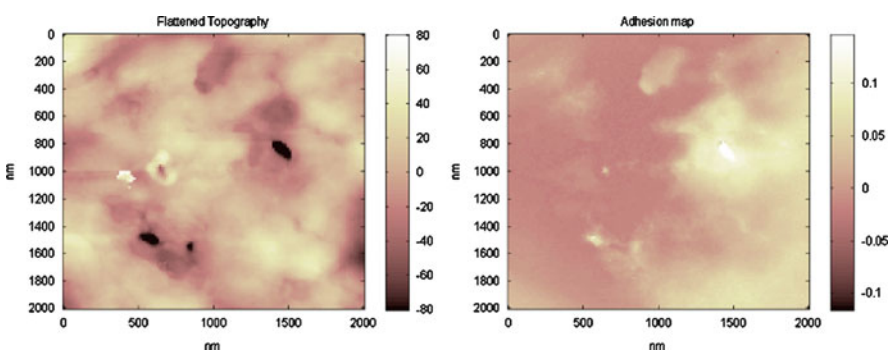


**Fig. 16.32** Images of the topography and adhesion maps of the force-volume application (Fig. 16.30)

On the basis of this model, they discuss the mechanisms, which determine the appearance of the experimentally acquired lateral force maps. Note the importance of topographic correction for corrugated samples. They present their topographic correction procedure in the framework of a complete quantitative statistical protocol based on AFM for the characterization of frictional properties of materials at the submicrometer scale and show the results of the application of the protocol used in this chapter to different materials. Stratum corneum fits the sample definition for the method introduced above.

Three different zones were selected for the frictions measurements. No phospholipid interaction is expected in the selected areas, and decent force curves can be achieved (Fig. 16.35).

this figure will be printed in b/w

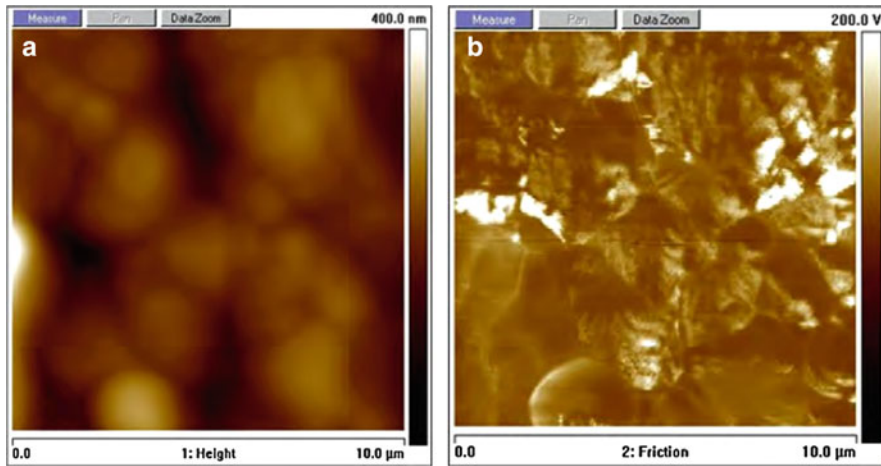


**Fig. 16.33** (a) Topography. (b) Subtracted lateral force images of stratum corneum, acquired with the colloidal probe

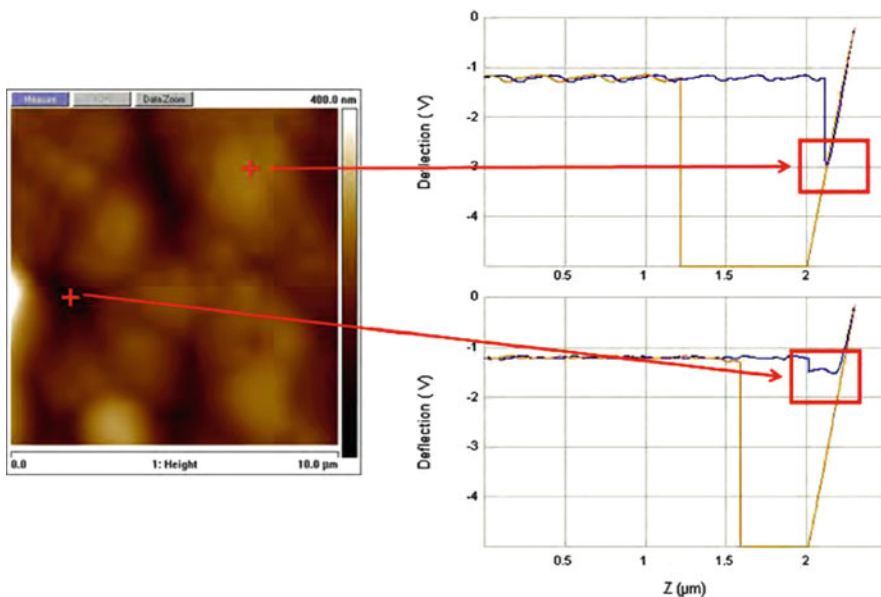


**Fig. 16.34** Observation of the plateau on the images acquired by the AFM using the colloidal probe

Friction varies considerably in  $1.1\text{-}\mu\text{m} \times 1.1\text{-}\mu\text{m}$  areas selected from a  $10\text{-}\mu\text{m} \times 10\text{-}\mu\text{m}$  area: In some areas,  $0.025 \pm 0.002$  is measured, in others, the maximum value is 0.006 (Fig. 16.36). The small coefficient of friction might be due to lipids

this figure will be printed in b/w

this figure will be printed in b/w

this figure will be printed in b/w

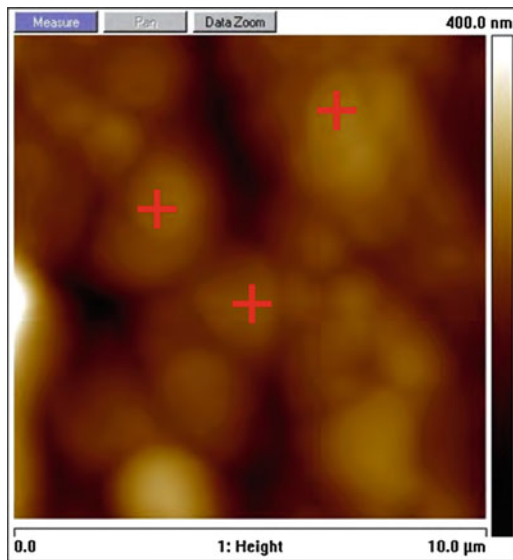


**Fig. 16.35** Selected areas for friction measurements

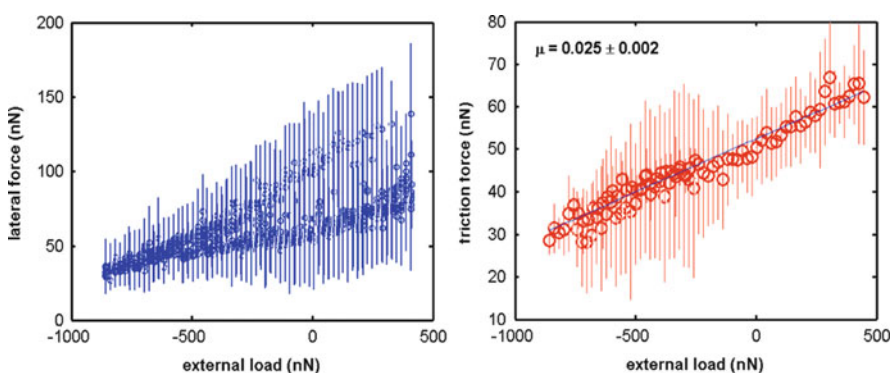


**Fig. 16.36** (a) Double trend in friction measurements. (b) Overlapping trend in two different areas

acting as lubricants. Topography and adhesion maps of such areas reveal that human skin exhibits significantly different phases on the micrometer scale (Fig. 16.37).

#### 16.3.4.4 Further Applications

The tests in this section were conducted in environmental conditions with 25°C temperature and 42.5% of relative humidity. Stratum corneum epidermis was also tested in a chamber with nitrogen flux providing dry conditions (RH: 0–5%) and with nitrogen and water flux providing wet conditions (RH: 90–95%) to better

this figure will be printed in b/w

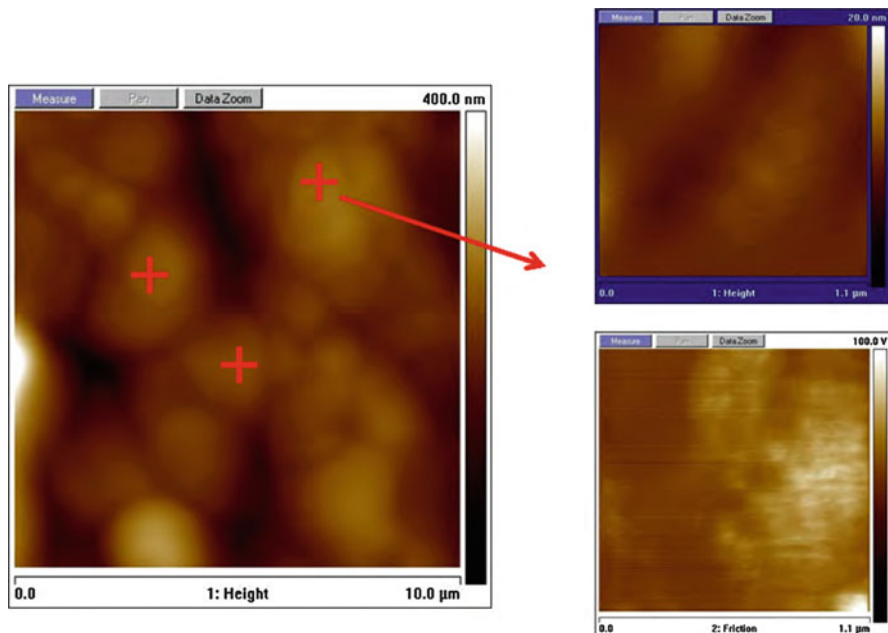


**Fig. 16.37** Topography and subtracted lateral force images of an area selected for friction measurements

understand the effects of environmental conditions and to observe contact area dependence related to colloidal probes of different sizes.

### 16.3.5 Staining Experiments Related to the Interactions Between Contact Lenses and Ocular Tissues

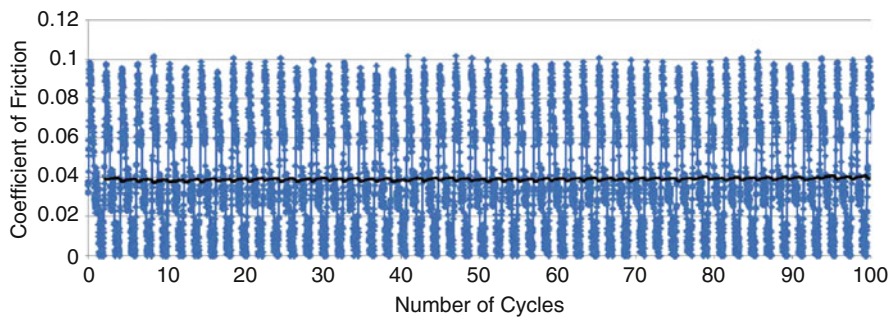
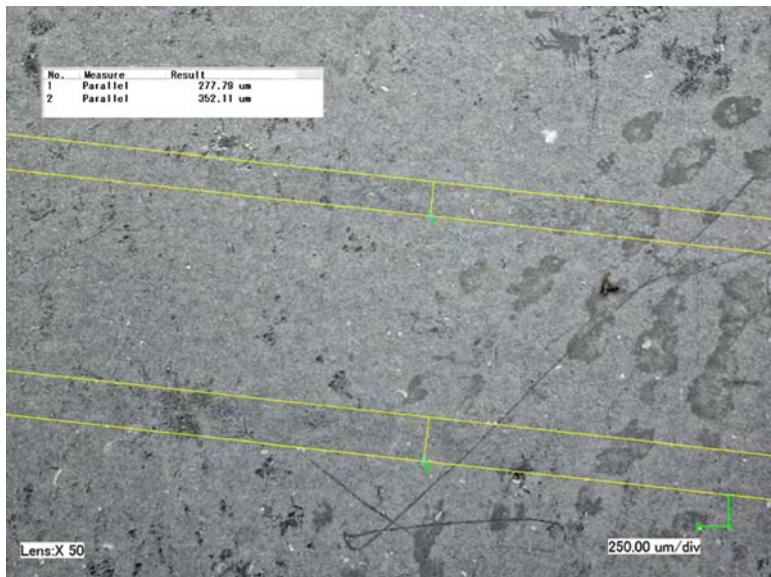
#### 16.3.5.1 Topography

Calibration tests of the system were performed on the endothelium biomimic, DSM-PTG CarboSil® 40 90A (biocompatible silicone polycarbonate urethane). CarboSil® combines the biocompatibility and biostability of conventional silicone elastomers with the processability and toughness of thermoplastic polycarbonate urethane (TPU).

The system allowed for repeatable and stable imaging, thereby encouraging continuing experiments on the cellular level (Fig. 16.38).

When the test was repeated with 1.2 and 2.0 mN, wear tracks with a width of 277 and 352  $\mu\text{m}$  were observed (Fig. 16.39).

this figure will be printed in b/w

**Fig. 16.38** Stable signal during 100 strokes**Fig. 16.39** Wear tracks recorded by optical microscopy related to the MTT tests with normal force values of 1.2 and 2.0 mN

If we consider constant contact pressure for both tests, we would expect

$$F_1/F_2 = (w_1)^2/(w_2)^2 \rightarrow (1.2)/(2.0) = 0.6 \approx 0.62 = (277.79)^2/(352.11)^2$$

The values are in good agreement with each other, yielding 20.55 kPa as first assumption of the contact pressure.

Further tests were conducted on HT-1080 muscle cells, derived from mouse uterus. These cells are selected for the tests due to their classification as Biosafety Level 1, significant resemblance with human samples, strong adherence to selected petri dishes and immortality ratios.

this figure will be printed in b/w

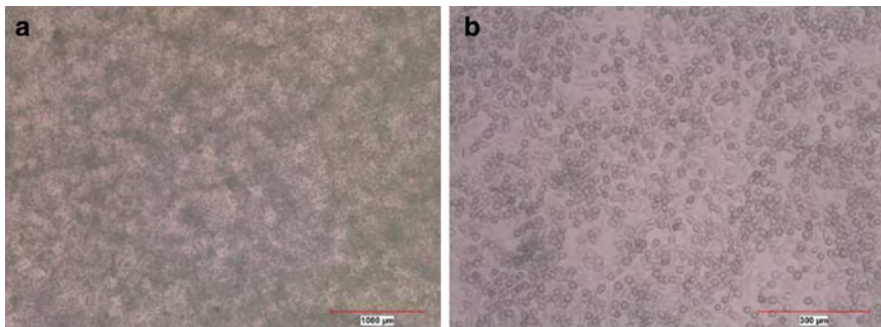


**Fig. 16.40** Cultured HT-1080 muscle cells under the optical microscope. (a) Scale bar 1,000  $\mu\text{m}$  and (b) scale bar 300  $\mu\text{m}$

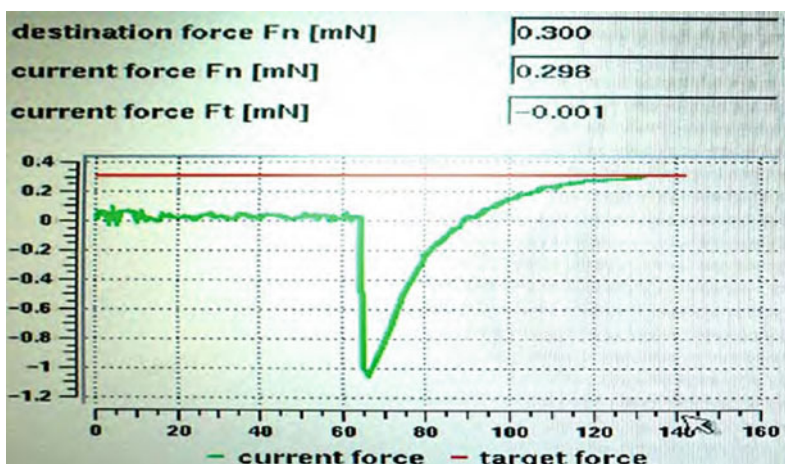


**Fig. 16.41** Force curve recorded during the approach of the tip to the cell line surface with a target force ( $F_t$ ) of 300 mN

The morphology of the muscle cells, cultured on Corning<sup>®</sup> culture dishes, represents pseudostratified simple epithelium properties that are similar to examples of liquid lubricant interfaces and sufficient to conduct the tribological tests (Fig. 16.40).

### 16.3.5.2 Force–Distance Plots

The force–distance plots acquired during the tests with the Falex MUST MTT revealed the issue concerning the meniscus and the tare force described in Sect. 16.2.3.3. In Fig. 16.41, a strong meniscus force of 1 mN can be observed during the approach of the tip to the cell lines.

this figure will be printed in b/w

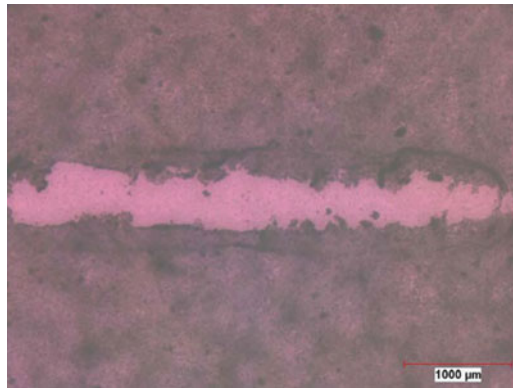


**Fig. 16.42** Complete wipe of cells under the exerted normal load of 1.3 mN. Scale bar 1,000  $\mu\text{m}$

The reason that the TARE function does not work after the tip totally dipped in to the buffer solution is that the meniscus force  $F_m$  is exerted in opposite direction to the forces that are recorded by the sensor as a result of the deflection of the cantilever. So the minus values of the deflection of the cantilever due to the pulling effect by the meniscus would not be nullified. In this case, the total force  $F_T$  exerted on the cell lines is

$$F_T = F_t + F_m = 0.3 + 1 = 1.3 \text{ mN}$$

This value of exerted normal load on cells is exceeding the adherence forces between the cells and the petri dishes, leading to complete wipe of the cells through the wear track (Fig. 16.42).

Subsequent to a software update on Falex MUST MTT, the total forces on both directions could have been tared to zero, and the actual value of the target force became the total force exerted on the cell lines. Proper friction measurements could be conducted and will be reported in the following section.

### 16.3.5.3 Friction Measurements

The initial tests conducted on HT-1080 muscle cells with a normal load of 0.3 mN show a partially stripped wear track (50–70% cell coverage) (Fig. 16.43a).

The probe velocity was 0.1 mm/s with a 3-mm single stroke. Results represent a stable friction force and similar coefficient of friction values for the first and the second pass of the stroke. This leads to the conclusion that insignificant or negligible ploughing occurs during the tests (Fig. 16.43b).

In Fig. 16.44, a slight deviation in the normal load values of the test can be observed. This effect is expected due to the small inclination on the surface of the petri dishes. Even though very stable values of friction force and coefficient of friction are acquired, for further application, a petri dish specially certified for

this figure will be printed in b/w

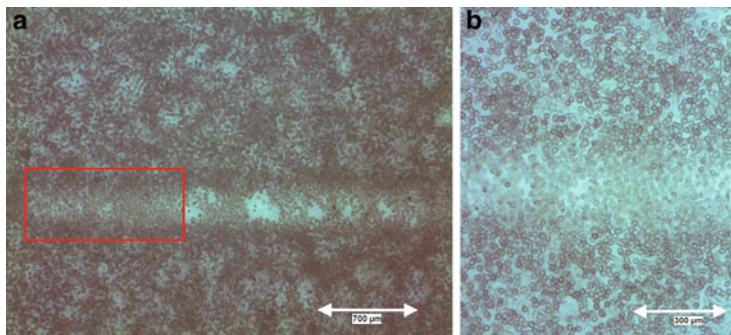


**Fig. 16.43** (a) Partially stripped wear track on cell lines with normal load of 0.3 mN, scale bar 700  $\mu\text{m}$ . (b) Zoom into the area marked with the red rectangle, scale bar 300  $\mu\text{m}$

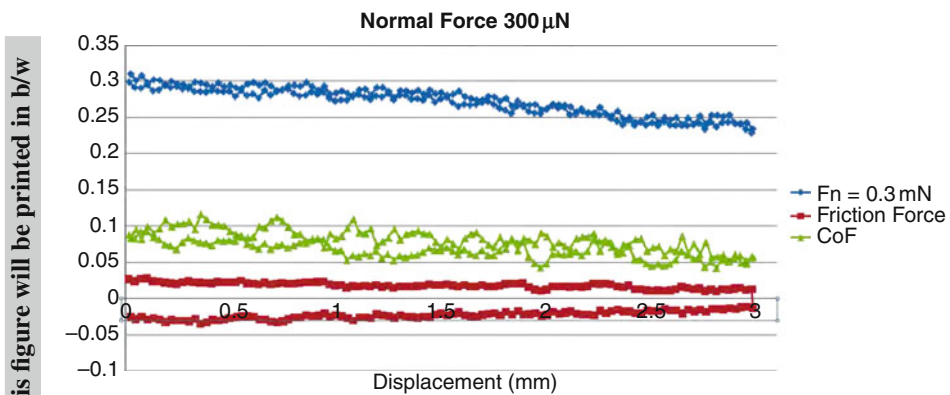


**Fig. 16.44** Normal force, friction force and coefficient of friction values for the test with assigned total force of 0.3 mN

flatness values is advised. The test was repeated with varying normal force values of 0.2, 0.5 and 0.7 mN.

From the friction results of five consecutive tests (marked as red squares in Fig. 16.45) it can be seen that friction behaviour and cell response are very similar to the studies of Sawyer with the coefficient of friction values varying stably between 0.008 and 0.11 considering 70–100% cell coverage [50].

#### 16.3.5.4 Further Applications

Following the success of the prototype universal experimental setup, the system was used for experiments on human corneal epithelium (HCE) after minor changes of the probe design. The general approach to the samples varies also due to the

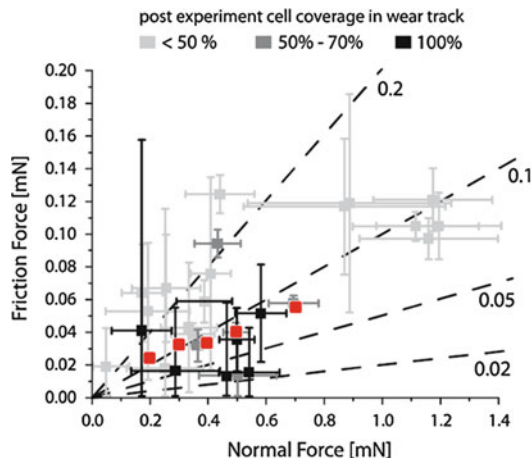


**Fig. 16.45** Comparison of results (red squares: 70–100% cell coverage) with Sawyer [50, 51]

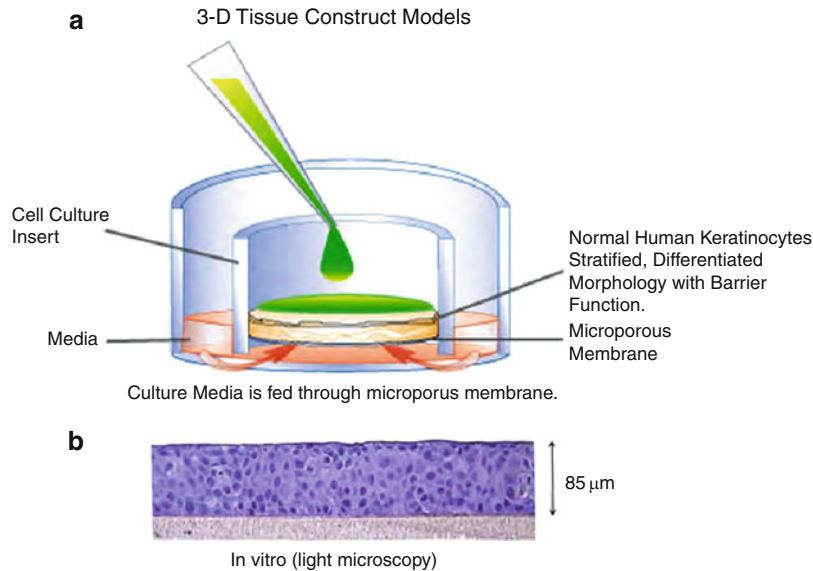


**Fig. 16.46** (a) Sketch of the tissue construction model. (b) *In vitro* light microscopy image of the constructed tissue

classification of HCE as Biosafety Level 2. Final applications envisaged would be 3-D tissue construct models from pseudostratified cell lines (Fig. 16.46).

When cultivated at the air-liquid interface in a chemically defined medium, the immortalized human corneal epithelial cells from the cell line HCE reconstruct a corneal epithelial tissue (mucosa), devoid of stratum corneum, ultrastructurally

(tissue morphology and thickness) similar to the corneal mucosa of the human eye [52]. This construction would provide a more stable base for the tests without sacrificing from the *in vitro* behaviour of actual human cornea. The tests would also be repeated for different kinds of contact lenses to evaluate efficiency and comfort of the products while reducing staining effect on the actual tissues. It is suggested to vary the tip diameter of the designed probe in order to investigate the contact area dependence of the system since the contact lenses are in touch with the corneal epithelia in more than one point, representing different models of contact.

## 16.4 Conclusion and Outlook: Bridging the Gap

In the sections above, measurements on two different kinds of surfaces were introduced. Chemisorbed monomolecular thin films of ethanolamines, ZnDDP tribofilms and hard coatings deposited by CVD or PVD were mainly investigated with scanning probe microscopy (atomic force microscopy, friction force microscopy) and angle-resolved photoelectron spectroscopy, whereas for the biomolecular layers, the methods of choice comprised scanning probe microscopy with a colloidal probe of several micrometres in diameter, a microtribometer, scanning electron microscopy and optical microscopy. The different questions asked in the respective studies require scientific investigations at different resolutions.

Scale effects need to be addressed when establishing tribological models across scales [53]. The type of instrument used depends on the questions that are addressed with the research. It is not always necessary (or even useful) to perform micro- or nanotribological investigations. Macrotribological investigations can give very useful general impressions of surfaces, without going too much into detail regarding distinct subparts. Certain indicators in macroscopic investigations allow for extrapolation to smaller scales – not in an exact way, of course, but in a timesaving way. Microtribological investigations yield important information concerning wear, surface fractures, the formation of structures between microscopic parts of the tribosystem and their boundaries (tensions, shears, rupture, deformation, etc.). On the nanoscale, molecular properties can be probed. Depending on the questions to answer, investigations on all three length scales (surfaces, clusters, molecules) might be necessary.

An interesting and challenging fact about tribology is that it is a systems science. Detailed understanding of a whole tribosystem is dependent on understanding of the connections, interdependences and single functionalities on all length scales of functionalities.

Due to increased specialization in science and engineering, many people work just in one small aspect of their respective field. Such specialists increasingly get to know their area better and better but in many cases have no time or think they have no reason to talk to specialists of related but slightly different fields. In the extreme, the specialist languages become too detailed, no joint language can be

reached across fields, and writings and oral presentations of authors only reach an audience coming from the same field.

If we are to understand tribosystems and to build models across scales that can perform the requirements we pose to models in science and technology, namely, to provide a way to predict the behaviour and performance of other, unrelated systems, knowledge transfer from one field of specialisation to the other needs to be ensured. Functionalities on the nanoscale influence functionalities on the microscale and subsequently on the macroscale. *What one hopes for is a unified approach to energy-dissipating systems that encompasses most tribological but also other phenomena, for example in biology and geology.* [54].

Three needs can be identified regarding successful development of such a unified approach to energy-dissipating systems: We need a joint language, a joint way of publishing results and joint seminars, workshops and conferences. Developing these three needs further results in a general concept concerning the future of scientific publications and ordering as well as accessing the knowledge of our time [55]. Currently, over-information in almost any field is a problem. Jack Sandweiss, editor of *Physical Review Letters*, stated in 2009 in an editorial address *For example, it is currently impossible for anyone to read all of Physical Review Letters or even to casually browse each issue.* [56]. Sandweiss refers to just one single journal!

Dynamic publications of variable length that use various types of multimedia with adaptive information content have been suggested [55]. One and the same paper would be accessible to readers from various backgrounds and areas of specialisation. In case more detailed information is needed, simple clicks on the links would expand the ‘paper’ in the direction(s) wanted. ‘Recommendation agents’ of the future could constrain information and thereby protect users from over-information by making the number of recommendations a function of the user’s ability and readiness information intake [55].

In this way, tribology generalists would emerge; people who ensure knowledge transfer from one area of specialisation to the other – contributing to a sound foundation to establish a unified approach to energy-dissipating systems across scales.

**Acknowledgements** The authors are grateful to the European Commission for supporting part of this work through their WEMESURF Marie Curie Research Training Network. The National University of Malaysia (Universiti Kebangsaan Malaysia) funded part of this work with its leading-edge research project scheme ‘Arus Perdana’.

## References

1. J.A. Greenwood, J.B.P. Williamson, Contact of nominally flat surfaces, Proc. Roy. Soc. Lond. A<sup>295</sup>, 300–319 (1966)
2. D. Tabor, Junction growth in metallic friction, Proc. Roy. Soc. Lond. A<sup>259</sup>, 378–393 (1959)

3. G.W. Stachowiak, A.W. Batchelor, in *Engineering Tribology*, 2nd edn. (Butterworth-Heinemann, Boston, 2001)
4. B. Bhushan, in *Handbook of Nanotechnology*, 2nd edn. (Springer, Berlin, 2003)
5. S. Bec, A. Tonck, J.M. Georges, R.C. Coy, J.C. Bell, G.W. Roper, A relationship between mechanical properties and structures of zinc dithiophosphate anti-wear films, *Proc. Roy. Soc. Lon.* **455**, 4181–4203 (1999)
6. P.A. Willermet, D.P. Dailey, R.O. Carter, P.J. Schmitz, W. Zhu, Mechanism of formation of antiwear films from zinc dialkyl dithiophosphates, *Tribol. Int.* **28**(3), 177–187 (1995)
7. H. Spedding, R.C. Watkins, Antiwear mechanism of ZDDP's—1, *Tribol. Int.* **15**(1), 9–12 (1982)
8. G.M. Bancroft, M. Kasrai, M. Fuller, Z. Yin, Mechanism of tribocochemical film formation: Stability of tribo- and thermally-generated ZDDP films, *Tribol. Lett.* **3**, 47–51 (1997)
9. P.A. Willermet, D.P. Dailey, R.O. Carter III, P.J. Schmitz, W. Zhu, J.C. Bell, D. Park, The composition of lubricant-derived surface layers formed in a lubricated cam/tappet contact II. Effects of adding overbased detergent and dispersant to a simple ZDTP solution, *Tribol. Int.* **28**, 163–175 (1995)
10. J.S. Sheasby, Z. Nisenholz Rafael, Antiwear characteristics of a commercial secondary ZDDP additives, *Tribol. Transact.* **36**, 399–401 (1933)
11. J.F. Graham, C. McCague, P.R. Norton, Topography and nanomechanical properties of tribocochemical films derived from zinc dialkyl and diaryl dithiophosphates, *Tribol. Lett.* **6**, 149–157 (1999)
12. B. Bhushan, in *Modern Tribology Handbook. Material Coatings, and Industrial Applications*, Vol. 2, 1st edn. (CRC Press LLC, Boca Raton, 2001)
13. M. Marieb, *Human Anatomy and Physiology*, 3rd edn. (Benjamin/Cummings, Redwood City, 1995)
14. J.A. Eurell, B.L. Frappier, *Dellmann's Textbook of Veterinary Histology*, 6th edn. (Wiley/Blackwell, Ames, 2006)
15. W. Ming, *Lasik Vision Correction* (Med World Publishing, Provo, 2000)
16. H. Kawano, H. Yasue, A. Kitagawa, N. Hirai, T. Yoshida, H. Soejima, S. Miyamoto, M. Nakano, H. Ogawa, Dehydroepiandrosterone supplementation improves endothelial function and insulin sensitivity in men, *J. Clin. Endocrinol. Metab.* **88**, 3190–3195 (2003)
17. O. Marti, J. Colchero, J. Mlynek, Nanosources and manipulation of atoms under high fields and temperatures, *Nanotechnology* **1**, 253–260 (1991)
18. G. Mayer, N.M. Amer, Simultaneous measurement of lateral and normal forces with an optical-beam-deflection atomic force microscope, *Appl. Phys. Lett.* **57**(20), 2089–2095 (1990)
19. B. Bhushan, *Nanotribology and Nanomechanics—An Introduction*, 2nd edn. (Springer, Berlin, 2005)
20. B.D. Beake, I.U. Hassan, C.A. Rego, W. Ahmed, Friction force microscopy study of diamond films modified by a glow discharge treatment, *Diamond Rel. Mat.* **9**, 1421–1429 (2000)
21. D.F. Ogletree, R.W. Carpick, M. Salmeron, Calibration of frictional forces in atomic force microscopy, *Rev. Sci. Instrum.* **67**(9), 3298–3306 (1996)
22. E. Tocha, H. Schonherr, G. Vancso, Calibration of frictional forces in atomic force microscopy, *Langmuir* **22**(5), 2340–2350 (2006)
23. M. Indrieri, A. Podestà, G. Bongiorno, D. Marchesi, P. Milani, Adhesive-free colloidal probes for nanoscale force measurements: Production and characterization, *Rev. Sci. Instrum.* **82**, 023708 (2011)
24. H. Oechsner (ed.), *Thin Film and Depth Profile Analysis. Topics in Current Physics*, Vol. 37 (Springer, Berlin, Heidelberg, New York, Tokyo, 1984)
25. R. Behrisch (ed.), *Sputtering by Particle Bombardment. Topics in Applied Physics*, Vol. 47 (Springer, Berlin, 1981)
26. A. Tomala, C.A. Vasko, N. Dörr, H. Störi, I.C. Gebeshuber, Oligomer specific lubrication, *Proceedings of the 34th Leeds-Lyon Symposium on Tribology*, Vol. 30, Lyon, 2007, pp. 2–3
27. A. Tomala, W.S.M. Werner, I.C. Gebeshuber, N. Dörr, H. Störi, Tribocochemistry of monomolecular lubricant films of ethanolamine oligomers, *Tribol. Int.* **42**, 1513–1518 (2009)

28. A. Tomala, A. Naveira-Suarez, R. Pasaribu, N. Doerr, W.S.M. Werner, H. Stoeri, Behavior of corrosion inhibitors under different tribological contact, *Tribol. Lett.* **45**, 397–409 (2012)
29. A. Naveira-Suarez, A. Tomala, R. Pasaribu, R. Larsson, I.C. Gebeshuber, Evolution of ZDDP-derived reaction layer morphology with rubbing time, *Scanning* **31**, 1–10 (2010)
30. H. Fujita, H.A. Spikes, The formation of zinc dithiophosphate antiwear films, *Proc. Inst. Mech. Eng. Part J J. Eng. Tribol.* **218**(4), 265–277 (2004).
31. A. Naveira-Suarez, A. Tomala, M. Grahn, M. Zacheddu, R. Pasaribu, R. Larsson, The influence of base oil polarity and slide-roll ratio on additive-derived reaction layer formation, *Proc. Inst. Mech. Eng. Part J J. Eng. Tribol.* **225**(7), 565–576 (2011)
32. M. Aktary, M.T. McDermott, G.A. McAlpine, Morphology and nanomechanical properties of ZDDP antiwear films as a function of tribological contact time, *Tribol. Lett.* **12**(3), 155–162 (2002)
33. K.A. Dean, B.R. Chalamala, Current saturation mechanisms in carbon nanotube field emitters, *Appl. Phys. Lett.* **76**, 375 (2000)
34. T. Zehnder, J. Patscheider, Nanocomposite TiC/a-C:H hard coatings. Deposited by reactive PVD, *Surf. Coat. Technol.* **138**, 133–134 (2000)
35. L.C. Wu, K. Miyoshi, R. Vuppuladhadium, H.E. Jackson, Physical and tribological properties of rapid thermal annealed diamond-like carbon films, *Surf. Coat. Technol.* **54–55**, 576–580 (1992)
36. R. Haubner, B. Lux, Diamond growth by hot-filament CVD: State of the art, *Diamond Rel. Mat.* **2**, 1277–1294 (1993)
37. K. Miyoshi, R.L.C. Wu, A. Garscadden, Friction and wear of diamond and diamondlike carbon coatings, *Surf. Coat. Technol.* **54/55**, 428–434 (1992)
38. J. Robertson, Diamond-like amorphous carbon, *Mat. Sci. Eng. R* **37**, 129–281 (2002)
39. P. Ovaere, S. Lippens, P. Vandenabeele, W. Declercq, The emerging roles of serine protease cascades in the epidermis, *Trends Biochem. Sci.* **34**(9), 453–463 (2009)
40. M. Haftek, S. Callejon, Y. Sandjeu, K. Padois, F. Falson, F. Pirot, P. Portes, F. Demarne, V. Jannin, Compartmentalization of the human stratum corneum by persistent tight junction-like structures, *Exp. Dermatol.* **20**(8), 617–621 (2011)
41. T. Igarashi, K. Nishino, S.K. Nayar, The appearance of the human skin: A survey, *Found. Trends Comp. Graph. Vis.* **3**(1), 1–95 (2007)
42. I.H. Blank, D.J. McAuliffe, Penetration of benzene through human skin, *J. Invest. Dermatol.* **85**, 522–526 (1985)
43. C. Soussen, D. Brie, C. Goboriaud, C. Kessler, Modelling of force volume images in atomic force microscopy, in *5th IEEE International Symposium on Biomedical Imaging: From Nano to Macro*, IEEE, Paris, 2008, pp. 1605–1608
44. B. Bhushan, in *Handbook of Micro and Nano Tribology* (CRC Press, Boca Raton, 1999)
45. G. Meyer, N.M. Amer, Simultaneous measurement of lateral and normal forces with an optical—beam—deflection atomic force microscope, *Appl. Phys. Lett.* **57**(20), 2089–2091 (1990)
46. M. Labardi, M. Allegrini, M. Salerno, C. Frediani, C. Ascoli, Dynamical friction coefficient maps using a scanning force and friction microscope, *Appl. Phys. A Solids Surf.* **59**, 3–10 (1994)
47. S. Sundararajan, B. Bushan, Topography-induced contributions to friction forces measured using an atomic force/friction force microscope, *J. Appl. Phys.* **88**, 4825 (2000)
48. A. Podestà, G. Fantoni, P. Milani, Quantitative nanofriction characterization of corrugated surfaces by atomic force microscopy, *Rev. Sci. Instrum.* **75**(5), 1228–1241 (2004)
49. F. Bowden, D. Tabor, in *The Friction and Lubrication of Solids* (Clarendon, Oxford, 1950)
50. A.C. Dunn, T.D. Zaveri, B.G. Keselowsky, W.G. Sawyer, Macroscopic friction coefficient measurements on living endothelial cells, *Tribol. Lett.* **27**, 233–238 (2007)
51. J.A. Cobb, A.C. Dunn, J. Kwon, M. Sarntinoranont, W.G. Sawyer, R. Tran-Son-Tay, A novel method for low load friction testing on living cells, *Biotechnol. Lett.* **30**, 801–806 (2008)
52. F.H. Kruszewski, T.L. Walker, L.C. Dipasquale, Evaluation of a human corneal epithelial cell line as an in vitro model for assessing ocular irritation, *Toxicol. Sci.* **36**(2), 130–140 (1997)

53. B. Bhushan, M. Nosonovsky, Scale effects in mechanical properties and tribology, in *Nanotribology and Nanomechanics—An Introduction*, 2nd edn., ed. by B. Bhushan (Springer, Berlin, 2008), pp. 791–840
54. M. Urbakh, J. Klafter, D. Gourdon, J. Israelachvili, The nonlinear nature of friction, *Nature* **430**, 525–528 (2004)
55. I.C. Gebeshuber, B.Y. Majlis, New ways of scientific publishing and accessing human knowledge inspired by transdisciplinary approaches, *Tribol. Surf. Mat. Interf.* **4**(3), 143–151 (2010)
56. J. Sandweiss, Essay: The future of scientific publishing, *Phys. Rev. Lett.* **102**(19), 190001(2p) (2009)